Effect of Rubber Particles and Fibers on the Dynamic Compressive Behavior of Novel Ultra-lightweight Cement Composites: Numerical simulations and Metamodeling

Zhenyu HUANG[1], Weixiong DENG[1], Shilin DU[1], Zewen GU[2], Wujian LONG[1], Jianqiao YE[2]*

1 Guangdong Provincial Key Laboratory of Durability for Marine Civil Engineering, Shenzhen University, Shenzhen, China 518060.

2 Department of Engineering, Lancaster University, Lancaster LA1 4YR, UK

Abstract

This paper presents, first, a finite element (FE) model for a rubberized ultra-lightweight cement composite (RULCC), which uses a modified Holmquist-Johnson-Concrete (H-J-C) constitutive law that is calibrated and validated by new Split Hopkinson pressure bar (SHPB) tests on the material. The validated FE model is used then as the core of a cloud computing platform using a multi node cloud simulation framework to carry out the parametric simulations, which generate required data to develop a meta-model to predict the dynamic impact strength of the RULCC. Design of experiment (DoE) and Generic Programming techniques are the main instruments in developing meta-models with reduced size of data. Finally, a meta-model of explicit expression, which is the first of its kind and considers the effect of rubber ratio, fiber ratio and dynamic impact strain rate, is proposed to predict the dynamic impact strength of the RULCC.

***Keywords*:** Rubberized concrete; Meta-model; Lightweight Concrete; Data driven; SHPB.

* Corresponding author: Email: j.ye@lancaster.ac.uk

1. Introduction

Addition of rubber particles into concrete aims to introduce a “soft” ingredient to improve the mechanical properties of the brittle material. The rubber particles are randomly distributed in the cement to absorb micro expansion and shrinkage, which reduces the brittleness of the concrete and improves its deformation compatibility. The mechanical performance of rubberized concrete is between that of normal and asphalt concrete. Therefore, it is called elastic or semi-rigid concrete. Extensive studies have found that rubberized concrete has many advantages, such as high toughness [1], high crack resistance [2, 3], high freeze-thaw resistance [4, 5], high impermeability resistance and high damping ratio [6-8]. It has been widely used in various engineering applications, such as highway pavement, structural retrofitting, and protective structures, etc [9-13]. It has greater potential to be used in marine structures, of which self-weight is one of the major concerns. Thus, lightweight and high-strength rubberized concrete with adequate ductility is a promising candidate [14-16].

The static compressive strength, tensile strength and elastic modulus of rubberized concrete decrease with the increase of rubber content, which has been confirmed by a large number of experimental studies [17-20]. The reduction in compressive strength is due to that: (1) rubber particles are organic polymers that have weaker bond strength in cement matrix [20]; and (2) the elastic modulus of rubber is much smaller than that of concrete. As a result, the added rubber particles in cement matrix are equivalent to distributed pores, which are prone to cause damage when the concrete is subjected to high stress [18]. To address this problem, Thomas et al. [20] added silica fume to rubberized concrete improve its compressive strength, which made the cement composite denser owing to the pozzolanic and filling effect of the silica fume. Some researchers modified the rubber with surface treating agent. Liu et al. [21] used NaOH and silane to pre-treat

45 the surface of waste rubber particles, which significantly improved the compressive and flexural
46 strength of the concrete. Because of the reduction in strength, some studies suggested that the
47 content of rubber particles should not exceed 20% [22]. The strength is not only related to the
48 amount of added rubber, but also to the size, the shape and the mechanical properties of the rubber
49 particles. In principle, the strength of rubberized concrete decreases as the size of the added rubber
50 particles increases [23]. Zheng et al.[24] replaced coarse aggregates by rubber particles of 2.6mm
51 and 4-15mm to study the effect of rubber size on the compressive strength, elastic modulus and
52 toughness index of concrete with rubber contents of 15%, 30% and 45% by volume [23]. Siddika
53 et al. [25] suggested that due to its low density and water absorption, waste rubber could be used
54 as aggregates for lightweight concrete in building structures.

55 Experimental studies have also been carried out to study the dynamics of rubberized concrete,
56 which have shown that both the rubber content and the particle size have significant impacts on
57 the dynamic behavior of the concrete. Increasing rubber content and decreasing rubber size in
58 concrete lead to greater strain rate and higher energy absorption capacity, which indicates a better
59 impact resistance. Guo et al.[26] investigated the strain rates of rubberized concrete with different
60 rubber contents. Under the same strain rate, the deformation capacity of a rubberized concrete
61 becomes higher as the added rubber content increases. Unlike the plain concrete, the failure of
62 rubberized concrete produces significantly larger concrete debris, indicating that the impact
63 resistance of rubberized concrete is higher than that of normal concrete. Dehdezi et al. [27]
64 developed a lightweight concrete with rubber powder replacement ratios of 20% and 50%, and
65 studied their energy dissipation capacity under impact loads. The addition of rubber to the normal
66 concrete represents a density reduction from 1823 kg/m^3 to 1680 kg/m^3 and 1582 kg/m^3,
67 respectively, achieving an increase of energy absorption at failure by 3.6 and 7.6 times. The

increases in energy absorption clearly demonstrate that the lightweight rubberized concrete has a much-improved energy dissipation capacity. Ali et al. [28] investigated the impact performance of a cement composite mixed with hybrid fiber (2% of polyvinyl alcohol-PVA and 1% shape memory alloy-SMA fibers) by drop hammer tests. The test results showed that the number of impacts the composite could receive before failure increased significantly, which indicated that the failure was more ductile, and the addition of fiber had effectively improved the impact performance of the cement composite. According to ACI 544 [29], Zhao et al. [30] carried out drop hammer tests on the concrete boards mixed with PVA fiber and rubber, respectively, and found that the impact resistance of the concrete was 8.3 and 1.3 times higher than that of normal rubber concrete. The fibers played an important role in the formation of concrete cracks while the rubber particles provided superior energy dissipation capacity. These studies have shown that rubberized concrete exhibits good impact resistance, which is particularly suitable for structures requiring high impact and seismic resistance. Moreover, the development and the applications of ultra-lightweight cement composite (ULCC) using fly ash cenospheres as lightweight aggregate have been extensively investigated. These studies include the investigations on the mechanical properties, functionalities and durability performance of ULCC [31], and on the flexural [32], shear [33], compression [14-15] and punching shear [34] behavior of ULCC filled sandwich composite structures. It was concluded that ULCC has excellent properties in mechanical, durability and structural performance, and has a wide range of industrial applications [35]. However, to the authors' best knowledge, the dynamic performance of ULCC has not been properly studied and well documented in the literature.

Though there has been significant research on the dynamics of rubberized concrete, they were rather scattered, thus providing, e.g., no simple and practical analytical formulas, which can take

into account fiber and rubber replacement ratio, to predict dynamic design characteristics of rubberized concrete, such as the dynamic strength and the dynamic increasing factor (DIF), etc. CEB-FIP 1990 proposed a DIF regression formula for different types of concrete , where DIF and strain rate are in a dual logarithmic relationship with the static compressive strength. The formula was further simplified in CEB-FIP 2010[36] for a specified range of strain rate, while the effect of the static compressive strength was ignored. Fig.1 summarizes the DIF for different types of concrete, where comparisons with the prediction curves of CEB-FIP[36, 37] and the published models[38-45] are also shown. The comparisons in the figure indicate that the CEB-FIP formulas are able to predict the DIF for some ordinary concretes but not for most of the lightweight concrete with rubber or/and fibers. One of the major issues of the existing formulas is that the rubber and fiber content ratios cannot be taken into account in the predictions. This is why they have failed to cover a range of lightweight concrete as the influence of rubber particles and fibers on the concrete dynamic performance is significant and should be considered, as illustrated by the test results in Huang et al. [46].

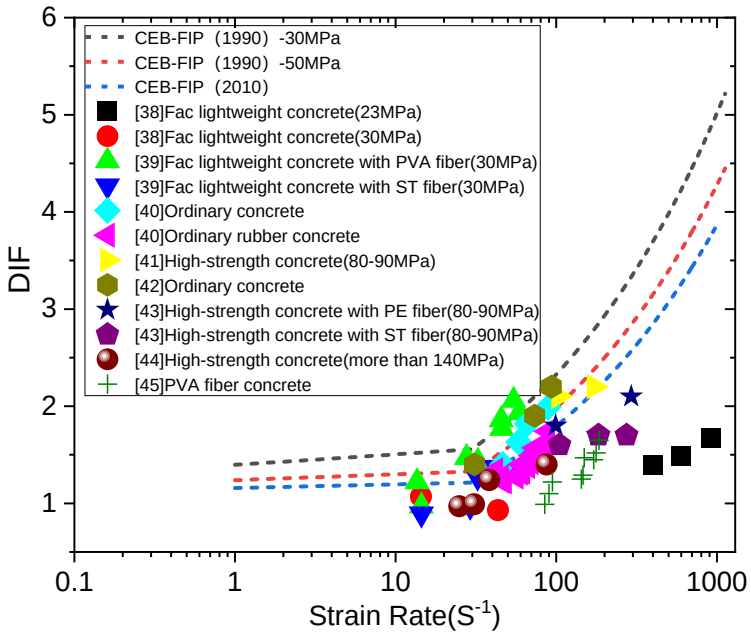

Fig.1 DIF of different types of concrete

From the above review and to the authors' best knowledge, the current impact design of rubberized concrete is largely based on simple models that were developed from regression of limited experimental data and cannot consider the effect of rubber and fiber contents. Though an advanced finite element (FE) modelling can be adopted for the purpose, it is not practically convenient for a practitioner engineer to implement a complex numerical model in a design process. There is a lack of validated design guidelines for performance-based design of rubberized concrete, and the calculations are still time-consuming and labor-intensive. Therefore, it is very urgent to develop a new efficient design method to predict dynamic performance of the material with proper consideration of their rubber and fiber contents.

The research reported in this paper has two main parts. The first part starts with an evaluation of the dynamic compressive stress-strain relationship and the damage modes of a novel lightweight (density of less than 1450kg/m^3) and high-ductility (direct tensile strain of 6%) cement composite with added rubber powder and low content PE fibers, using Split Hopkinson Press Bars (SHPB) tests. The test results, including the failure modes, are used next to validate a FE model that is developed in LS-DYNA using a modified H-J-C constitutive law. The validated model is then used to carry out a series of parametric studies to test the effect of the fiber and rubber content ratios on the performance and failure of the composite. The second part of the research is to propose a data-driven modelling process, from which a simple analytical formula to predict dynamic strength of the material is obtained with a full consideration of the replacement ratios of fibers and rubber, as well as the impact strain rates. With the help of design of experiments (DoE) sampling technique, an optimized pool of date points, each of which represents a design of the material, is established to minimize the computational cost. Full FE analyses are carried out to

obtain the dynamic strength of each of the sampling design using a Multi-Node Cloud Simulation Framework. On the basis of the experimental and numerical results, an explicit meta-model for the dynamic strength is developed through training the DoE selected design using generic programming (GP). The new formula considers the strain rate effect, fiber content and rubber content in the model to predict the dynamic strength of the ultra-lightweight rubberized cement composite. The predictions from the formula are finally compared with independent designs from the FE simulations. This study offers a new route for performance-based dynamic design of rubberized cement composite, the principle of which can be extended to the material design in other similar research areas.

2. Experimental data for model validation

2.1 The rubberized material

The novel rubberized ultra-lightweight high ductility cement composite (RULCC) to be modelled is composed of cement, fly ash cenospheres (FAC), silica fume, rubber powder aggregates and polymer polyethylene (PE) fibers. The RULCC has a target 28-day compressive strength around 35MPa with a low density of around 1450kg/m^3. Table 1 details the mix proportions of the RULCC. The RULCC matrix has a water-to-binder ratio of 0.37 to achieve a high strength. The binder consists of 100% of CEM I 52.5R ordinary Portland cement and 11 wt% of silica fume and 38.7-48.4wt% FAC. The rubber powder to partially replace the FAC is of 380μm in diameter. Further details about the manufacturing process of the materials can be found in Huang et al. [46]. To evaluate the properties of the material, the mixes with seven different rubber and fiber contents were tested in Huang et al. [46], as listed in Table 1, which includes the replacement ratios of rubber contents (5%, 10%, 15% and 20%) and fiber contents (0% and 0.7%). The mechanical properties of the PE fibers are shown in Table 2.

Table 1 Mix proportions of RULCC

Mix ID	Cement	SF	FAC	Rubber	Water	SP	SRA	Fiber
R0-0	1	0.11	0.484	0.000	0.37	0.001	0.001	0
R5-0	1	0.11	0.460	0.027	0.37	0.001	0.001	0
R10-0	1	0.11	0.436	0.054	0.37	0.001	0.001	0
R15-0	1	0.11	0.412	0.080	0.37	0.001	0.001	0
R20-0	1	0.11	0.387	0.107	0.37	0.001	0.001	0
R0-0.7PE	1	0.11	0.484	0.000	0.37	0.001	0.001	0.7%
R10-0.7PE	1	0.11	0.436	0.054	0.37	0.001	0.001	0.7%

Note: SF=silica fume; FAC=fly ash cenospheres; SP= superplasticizer; SRA= shrinkage reducing agent.
R10-0.7PE represents the RULCC with 10% rubber powder replacement of FAC and 0.7% PE fiber by volume.

Table 2 Mechanical properties of surface treated PE fiber

Diameter (μm)	Length (mm)	Density (g/cm^3)	Tensile strength (MPa)	Elastic modulus (GPa)	Fracture elongation (%)
24	12	0.97	3000	120	2-3

2.2 SHPB test

The static compression test was performed by using a 300 tone MTS machine to compress Φ100x200 concrete cylinders, according to ASTM C39/C39M[47]. Uniaxial static tensile test was carried out in accordance with the standard recommended by JSCE [41]. To investigate the dynamic behavior of the RULCC, Split-Hopkinson pressure bar was used to test the material under impact loads. Fig.2 shows the setup of the SHPB tests. The seven groups of the specimens listed in Table 1 were loaded to four different strain rates relative to four different air pressures, i.e., 0.2MPa, 0.3MPa, 0.4MPa and 0.5MPa, respectively.

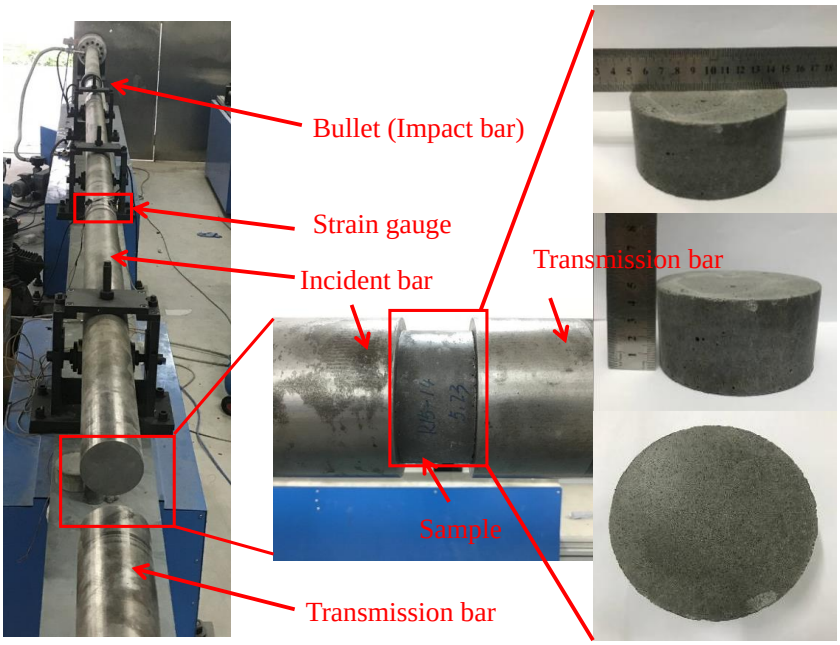

Fig. 2 Split Hopkinson Pressure Bar and test sample

Fig. 3 shows the failure process of the RULCC which was captured by a high-speed camera. The pictures were taken at several intervals within 0.0015 seconds from the start of the impact (from left to right). Among them, Figs. 3 (a)-(b) show the failure of the RULCC with rubber contents of 0% and 15%, respectively. Fig. 3(c) shows the failure of the RULCC with 10% rubber and 0.7% PE fibers. Figs. 3(d) shows the failure process of the RULCC with different rubber replacement ratios under a pressure of 0.3MPa. Multiple cracks on the surfaces of the specimens were found immediately after the RULCC was impacted, as shown in Figs. 3 (a) and (b). Due to the greater deformation and energy absorption capacity of the rubber, part of the impact energy can be dissipated timely, thus initiating a reduced number of cracks, but increased size of fragments. This phenomenon is more pronounced as more rubber powder are added. It is worth noting that compared with Figs. 3(a) and (b) at 0.00025 s, multiple cracks appear in the specimens without rubber. However, fracture of R15-0 is not obvious when the air pressure is lower than 0.3MPa, and only a few small cracks appear when the air pressure is greater than 0.3MPa. This shows that the addition of rubber powder can effectively delay the development of cracks, which demonstrates

that the specimens absorb part of the impact energy through the increased deformation, resulting in larger and less fragments. For the specimens with a low fiber content of 0.7%, though there are many micro cracks formed at a low strain rate, the final failure is triggered by only one main crack, while the integrity of the specimen is still maintained, as shown in Fig. 3(c).

Figure 4 shows the Scanning Electron Microscopy (SEM) images of the damaged R0-0 and R0-0.7PE, showing the crushing of the cenospheres in the R0-0 and fiber pulling-out in the R0-0.7PE. Under a high compressive impact, the RULCC without fails due to cenosphere crushing rather than matrix failure, which is similar to the failure mode of the material under static compressive loading. However, for the R0-0.7PE, the failure mode is fiber pulling-out from the cement matrix, which is different. A small portion of the cement matrix is still adhered to the fibers, indicating the fibers and the cement matrix are still well-bonded. This indicates that the addition of fiber leads to the changes in the failure mechanism of the RULCC from brittle cenosphere crushing to ductile fiber pulling-out, which dissipate more energy in the process. This also indicates that the fiber plays a positive role in improving the damage morphology under high strain rate impact.

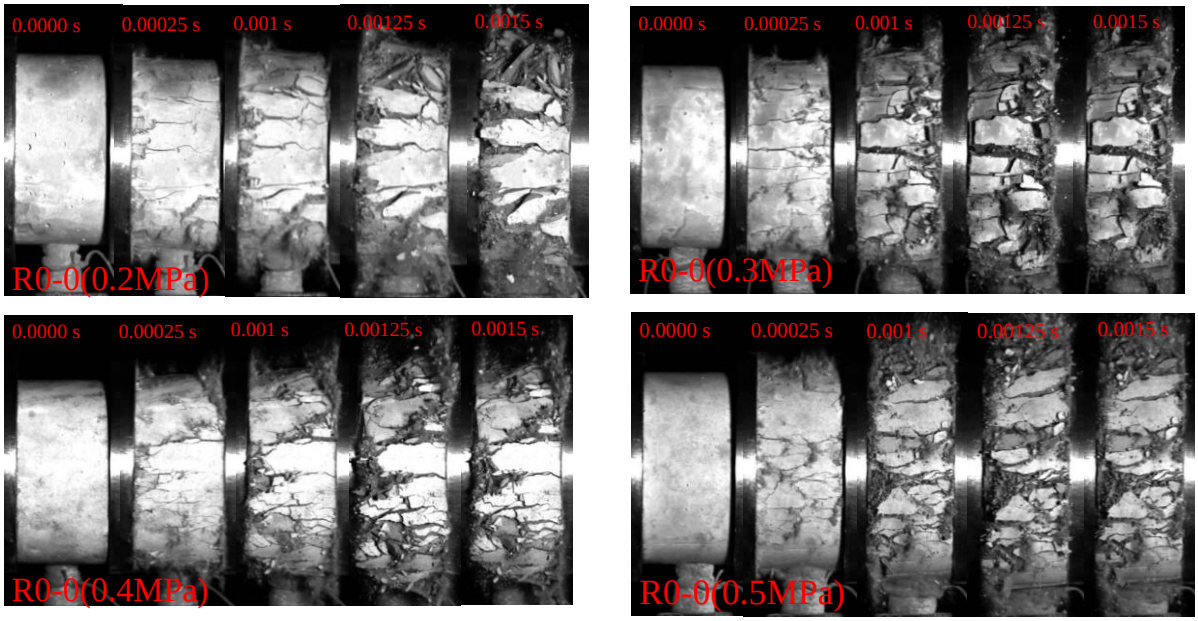

(a) R0-0

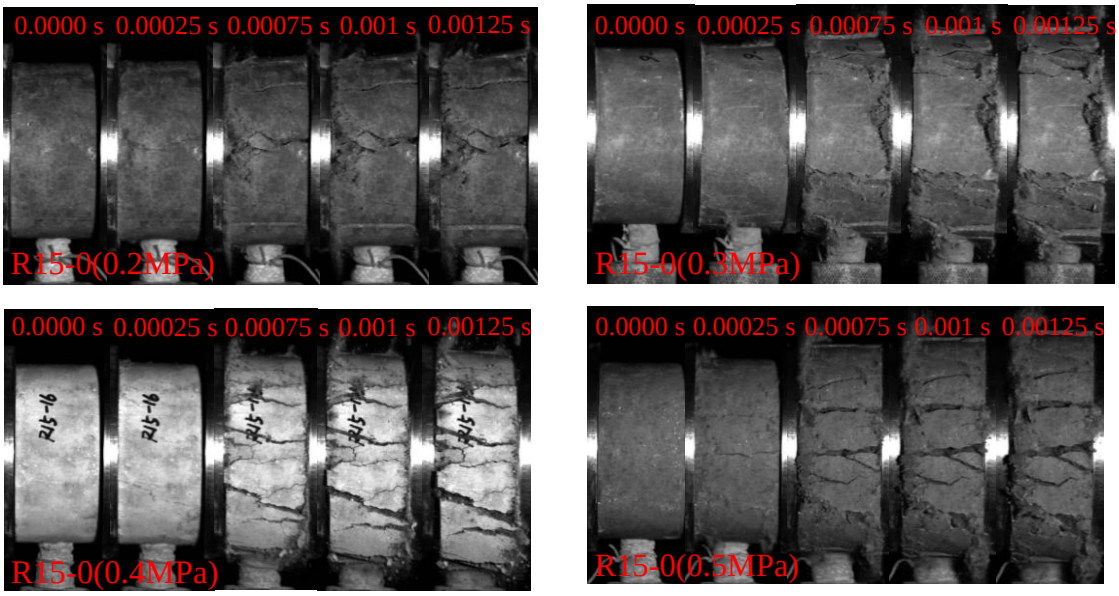

197 (b) R15-0

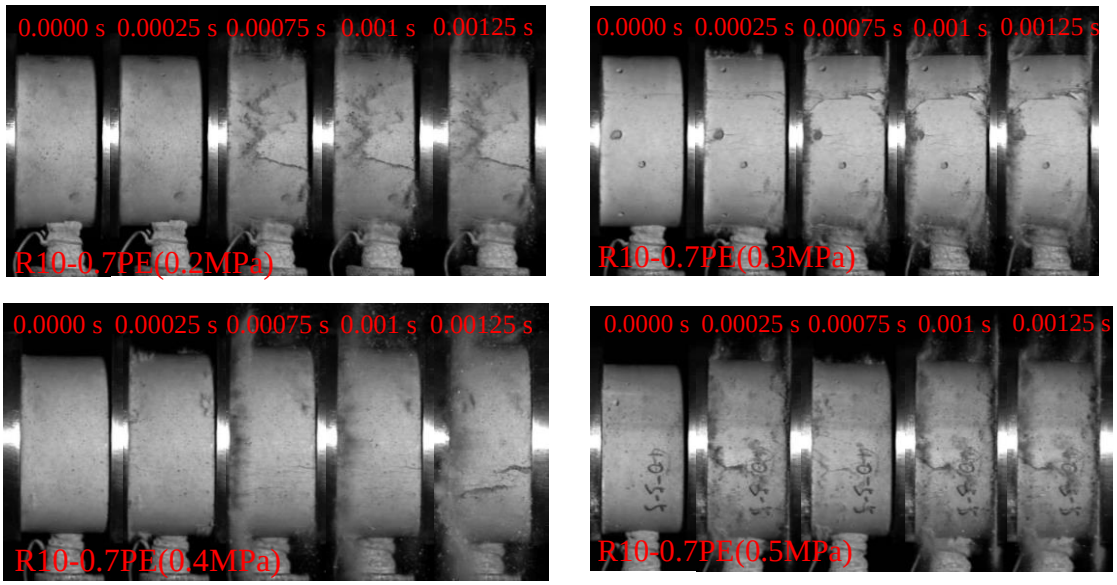

198 (c) R10-0.7PE

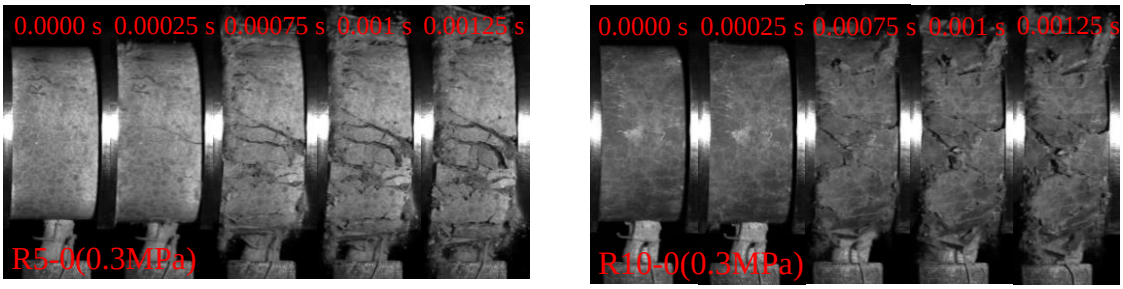

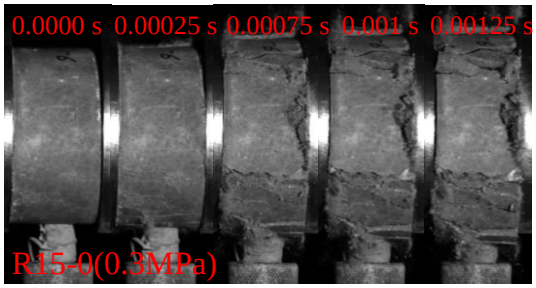

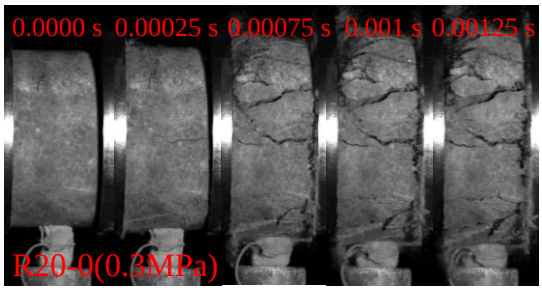

(c) RULCC (0.3MPa)

Fig. 3 Failure process of RULCC

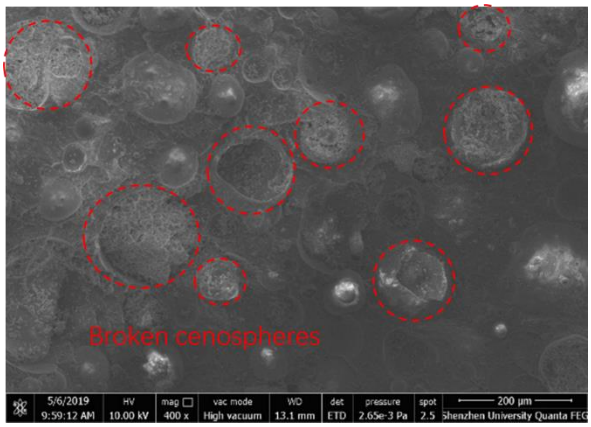

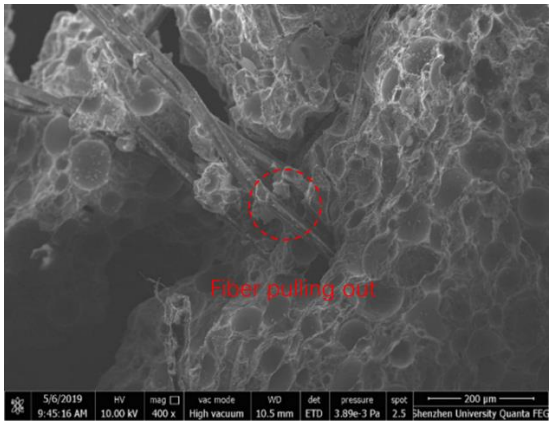

(a) Cenospheres crushing-R0-0 (b) Fiber pulling out-R0-0.7PE

Fig. 4 SEM photo of RULCC with/without fibers (under 0.5MPa pressure)

More detailed and the insight studies of the experiments and the results can be found in Huang et al. [46]. The numerical data from the tests are used in the following section to develop and validate the numerical models.

3. Numerical simulation

3.1 Finite element modeling

3.1.1 H-J-C constitutive model

This section simulates the SHPB impact tests of the RULCC using the explicit codes in LS-DYNA[48]. The material properties of the SHPB steel bar adopt the J2 plasticity model (type MAT_24). The properties of the RULCC utilize the Holmquist-Johnson-Concrete (H-J-C) model

that can present the dynamic compressive behaviour of concrete well when the concrete is subjected to high strain rate impact[49]. Adopted also by some other researchers[50, 51] to simulate cementitious composites under dynamic loadings, this model considers the effect of large strain, high strain rate and high pressure using both Lagrange and Euler meshes. The H-J-C model consists of three parts, namely, the strength model, the damage evolution equation and the state equation. The strength model of H-J-C is defined in terms of the normalized parameters, as shown in Fig.5, which is underpinned by Eq.(1) below,

$$\sigma^* = [A(1-D) + BP^{*N}][1 + C\ln(\dot{\varepsilon}^*)] \quad (1)$$

where, A, B, C and N are material constants; σ^* is the normalized effective strengh, $\sigma^* = \sigma / f_c \le S_{\max}$ and $S_{\max}$ is the normalized maximum strength; f_c is the uniaxial compresive strength; $P^* = P / f_c$ is the normalized pressure; $\dot{\varepsilon}^* = \dot{\varepsilon} / \dot{\varepsilon}_0$ is the effective strain rate, $\dot{\varepsilon}$ is the true strain rate while $\dot{\varepsilon}_0 = 1.0s^{-1}$ is the reference strain rate; $T^* = T / f_c$ and T is the maximum tensile strength of the concrete.

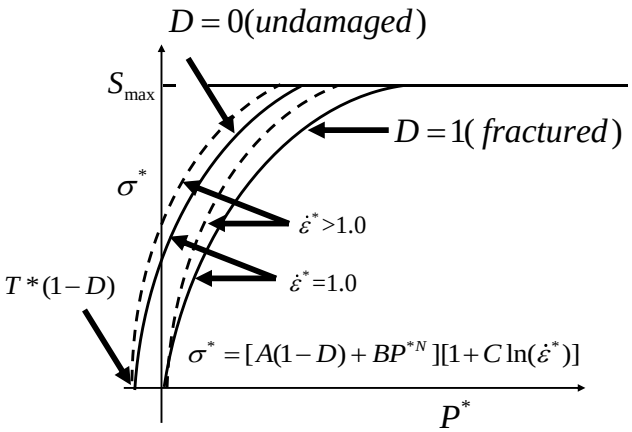

Fig.5 H-J-C strength model

The damage specified by the H-J-C model evolves from plastic strain accumulation, as shown in Fig. 6. The plastic strain includes the equivalent plastic strain and the plastic volume strain. The damage evolution equation is as follows,

$$D=\sum\frac{\Delta\varepsilon_p+\Delta\mu_p}{\varepsilon_p^f+\mu_p^f} \tag{2}$$

$$\varepsilon_p^f+\mu_p^f=D_1(P^*+T^*)^{D_2} \tag{3}$$

where, D_1 and D_2 are damage constants; D denotes damge factor, $D\in[0,1]$; $D_1(P^*+T^*)^{D_2}\geq\varepsilon_{f,\min}$, $\varepsilon_{f,\min}$ is the minimum fracture strain that can be determined by a tensile test; $\Delta\varepsilon_p$ and $\Delta\mu_p$ represent the effective plastic strain and plastic volume strain, respectively, for the element at each integral step; $\varepsilon_p^f+\mu_p^f$ is the plastic strain at the current integration step.

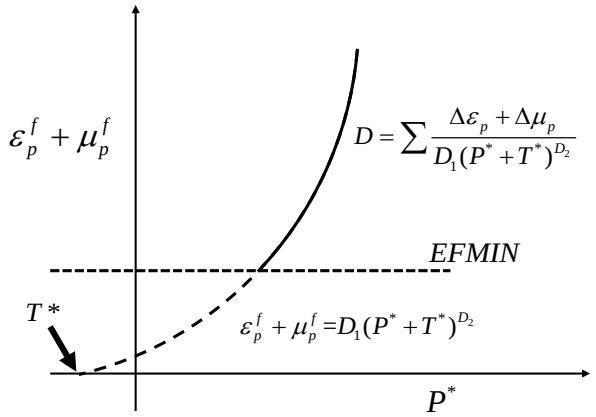

Fig. 6 Material damage evolution relationship

The state equation is used to describe the relationship between the volume strain and the hydrostatic pressure. The state equation of the H-J-C model is divided into three stages, i.e., elastic, transition and compaction stages, as shown in Fig.7. The first stage ($-T(1-D)\leq P\leq P_{crush}$) is linear elastic, and the relationship between the hydrostatic pressure P and the volume strain is as follow,

$$P=K\mu \tag{4}$$

where, P is the hydrostatic pressure; K is the bulk modulus; μ is the volume strain; P_{crush} is the hydrostatic pressure at elastic limit.

The second stage ($P_{crush} < P \le P_{lock}$) is the transition stage, in which the voids in the material is gradually compacted to produce plastic deformation. The loading and unloading equations are as follows,

$$P=\frac{(\mu-\mu_{crush})(P_{lock}-P_{crush})}{\mu_p-\mu_{crush}}+P_{crush} \tag{5}$$

$$P=P_0-\left[(1-F)K+FK_1\right](\mu_0-\mu) \tag{6}$$

$$F=\frac{\mu_0-\mu_{crush}}{\mu_p-\mu_{crush}} \tag{7}$$

where, μ_p is the volume deformation corresponding to the compaction hydrostatic pressure P_{lock}; P_0 is the hydrostatic pressure corresponding to the volume deformation μ_0 before unloading; F is the unloading proportionality coefficient.

The third stage ($P_{lock} < P$) is the pore free compaction stage, during which the material has been completely damage. The loading and unloading equations are as follows:

$$P = K_1\bar{\mu} + K_2\bar{\mu}^2 + K_3\bar{\mu}^3 \tag{8}$$

$$P = K_1\bar{\mu} \tag{9}$$

$$\bar{\mu}=\frac{\mu-\mu_{crush}}{1+\mu_{lock}} \tag{10}$$

where, μ_{lock} is the volume strain at the compaction limit; $\bar{\mu}$ is the modified volume strain, which is to prevent the material from softening when it just enters the third stage; K_1, K_2 and K_3 are the pressure constants.

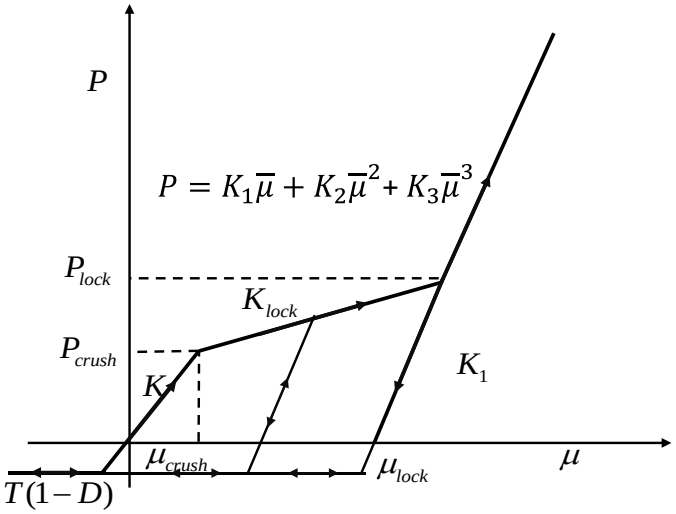

Fig.7 Pressure-volumetric strain curve

To reduce the computational costs without sacrificing the accuracy, the absorption rod is not included in the FE model. Hence, the model includes the impact bullet, the incident bar, the concrete samples and the transmission bar. The incident and transmission bars as well as the cement composite are meshed using the eight-node solid elements with reduced integration and hourglass control. Fig.8 is an illustration of the full-scaled FE model in the numerical analysis. The concrete sample is sandwiched between the two SHPBs to represent the boundary conditions in the test.

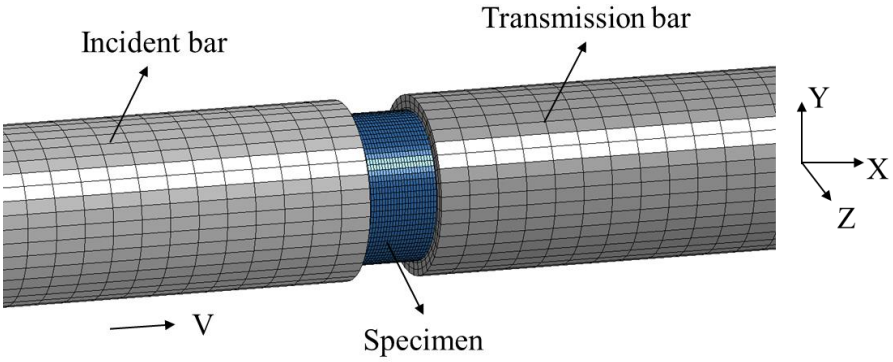

Fig.8 Full-scaled FE model for concrete under SHPB test

The interfaces between the SHPBs and the specimens are simulated by the surface-to-surface contact with a penalty algorithm. For the two deformable surfaces in contact, the master surface usually refers to the stiffer one or the surface with a coarser mesh if the two surfaces have comparable stiffness. Therefore, the FE model selects the SHPBs surfaces as the master surface.

The impact loads are simulated by changing the impact velocities of the bullet on the SHPBs. Fig.9 shows the input waves obtained from the tests and those from the simulations. It can be seen that both the strains measured from the SHPB tests and from the FE analysis agree very well, which demonstrates that the predicted input waves are sufficiently accurate.

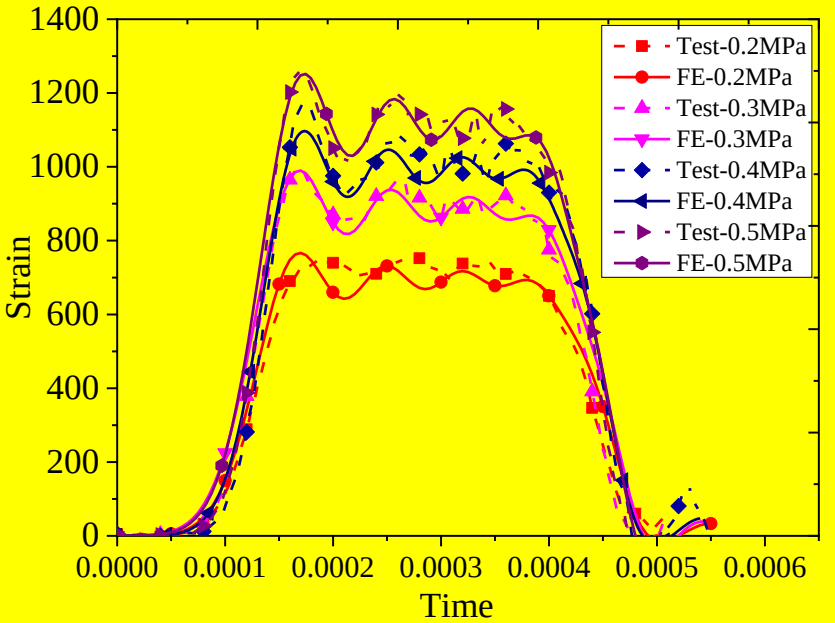

Fig.9 Validation between FE simulation and test for incident wave

3.1.2 Optimized H-J-C model

The Holmquist-Johnson-Cook (HJC) constitutive model is a dynamic model for concrete, as it considers pressure, strain-rate-dependent strength and void crushing damage. For the RULCC with fibers and rubber, due to the changes in the dynamic strength, the H-J-C model for concrete has to be modified, so that it can take into account the toughness and strength of the novel RULCC.

Some researchers[52-54] have considered the influence of the strength and toughness of the fiber, and introduced reinforcement factors to adjust the yield surface equation. In this study, a normalized cohesive strength influence factor α, and a normalized pressure hardening influence factor β, are proposed to represent the characteristic parameters of the PE fibers and the size of the rubber. It is also assumed that the effect of these two materials on the RULCC is linear as shown in Eqs.(11) and (12).

$$\alpha = a \cdot \frac{V_{PE} l_{PE}}{d_{PE}} - b \cdot M_r V_r \tag{11}$$

$$\beta = c \cdot \frac{V_{PE} l_{PE}}{d_{PE}} - d \cdot M_r V_r \tag{12}$$

where, V_{PE} is the PE fiber content in volume; l_{PE} is the PE fiber length; d_{PE} is the PE fiber diameter; M_r is the rubber size (test sieve of M_r=40 mesh according to ASTM E11-01[55], which is 380 μm in size in this study); V_r is the rubber content in volume. The four constant coefficients in Eq.(11) are determined by binary regression on the experimental results presented in [56], which are, respectively, a=0.3016, b=0.0239, c=0.2997, and d=0.0247. Thus, Eq.(1) is modified by introducting the two fiber- and rubber-dependent parameters from Eq.(11) and Eq.(12), as presented in Eq.(13). The original state and the damage evolution equations of the H-J-C model stay the same in the following simulations.

$$\sigma^* = [\alpha A(1-D) + \beta B P^{*N}][1 + C \ln(\dot{\varepsilon}^*)] \tag{13}$$

3.1.3 Determination of H-J-C model parameters

There are 21 material parameters in the original H-J-C constitutive model. Some of the material parameters can be calibrated by experiments, while the remaining parameters are obtained from calculations or the defalult values recommended by the software. Table 3 lists the parameters of the modified H-J-C model for the RULCC in the FE simulation. According to Wu et al.'s work[57] ,

$\varepsilon f_{\min}$ is determined by using the peak strain of the quasi-static state under low strain rate loading. Based on the parametric study, it is noted that $\varepsilon f_{\min}$ has little influence on the FE results. Therefore, for all the models in this study, the default value $\varepsilon f_{\min}$=0.01 is selected for the RULCC with and without fibers. S_{max} uses the defaut value of 7.0MPa in the H-J-C model [58], which is recommended by other researchers[59, 60]. The crush stress p_{cursh} under uniaxial compression is given by,

$$p_{cursh} = f_c / 3 \tag{14}$$

According to Holomquist et al.[61], the volume strain, μ_{crush}, is related to p_{crush} by,

$$\mu_{cursh} = p_{cursh} / K \tag{15}$$

in which, the volume modulus K is determined by,

$$K = \frac{E}{3(1-2\nu)} \tag{16}$$

P_{crush} is the compaction stress of the concrete shown in Fig 7, which is between 0.8-1.2MPa according to previous investigations [61, 62].

The volume strain μ_{lock} at full compaction is,

$$\mu_{lock} = \frac{\rho_{grain}}{\rho_0} - 1 = \frac{V_0}{V_g} - 1 = \frac{w}{1-w} \tag{17}$$

where, ρ_{grain}, ρ_0, V_g, V_0 and w are compaction density, initial density, compaction volume, initial volume and porosity ratio of the concrete, respectively. It should be noted that for lightweight cocnrete, the porosity ratio w is high and of 28%-50% [63].

It is not recomended to use the compact desity of light weight concrete in the above calculations since its high porosity may cause early concrete crush before being fully compacted, which is different to the copaction of normal weight cocnrete with low porosity. Therefore, the cement matrix densities, ρ_{grain} and ρ_0, are used instead. From Eq.(17), μ_{lock} can be expressed as

330 $\frac{V_0}{V_g}-1=\frac{w}{1-w}$, where V_0 and V_g are the initial volume and the volume after compaction of cement

331 matrix, respectively. From Li and Huang's investigation[64], the porosity ratio of hardened cement

332 matrix with a W/C of 0.3 to 0.4 are between 11.21% and 12.63%. Hence, the porosity of the ULCC

333 matrix with a W/C of 0.34 in this paper can be obtained by interpolation. f_s takes the value in Li[65]

334 or 0.004 as proposed by Liu et al.[11]. T is the tensile strength of lightweight concrete from tensile

335 test or Eurocode 2[66] , which is,

336 $$T=\eta_1 f_{ctk} \tag{18}$$

337 $$\eta_1=0.04+0.6\frac{\rho}{2200} \tag{19}$$

338 in which, f_{ctk} is the concrete strength from Table 3.1 in Eurocode 2; η_1 is the reduction factor; ρ

339 represents the upper limit of concrete density in accordance with Table 11.1 in Eurocode 2.

340 The elasatic modulus, E_c, of the ULCC was measured by experiments [67] in accordance with the

341 ASTM C469/C469M[68]. The shear modulus G is then obtained by,

342 $$G=\frac{E_c}{2(1+\nu)} \tag{20}$$

343 where ν is taken from the test results in reference[67]. The parameters of the modifed H-J-C model

344 are shown in Table 3.

Table 3 Parameters of the modified H-J-C model

Material	R0-0	R5-0	R10-0	R15-0	R20-0	R0-0.7PE	R10-0.7PE
Density ρ (kg/m^3)	1395	1397	1399	1401	1403	1405	1409
G (GPa)	5.833	4.917	4.125	3.958	3.875	4.958	4.125
A	0.54	0.56	0.50	0.48	0.46	0.57	0.48
B	2.25	2.25	2.20	2.18	2.15	2.36	2.09
C	0.007	0.007	0.007	0.007	0.007	0.007	0.007
N	1.36	1.36	1.36	1.36	1.36	1.36	1.36
f_c (MPa)	52.2	36.8	27.3	23.6	20.7	43.5	24.9

T (MPa)	2.4	1.9	1.6	1.4	1.3	2.1	1.4
$\dot{\varepsilon}_0$	1	1	1	1	1	1	1
εf_{min}	0.01	0.01	0.01	0.01	0.01	0.01	0.01
S_{max}	7	7	7	7	7	7	7
P_{cursh} (MPa)	17.40	12.27	9.10	7.87	6.90	14.50	8.30
μ_{cursh}	0.002237	0.001871	0.001655	0.001491	0.001335	0.002193	0.001509
P_{lock} (GPa)	0.9	0.9	0.9	0.9	0.9	0.9	0.9
μ_{lock}	0.12	0.12	0.12	0.12	0.12	0.12	0.12
D_1	0.04	0.04	0.04	0.04	0.04	0.04	0.04
D_2	1	1	1	1	1	1	1
K_1 (GPa)	85	85	85	85	85	85	85
K_2 (GPa)	-171	-171	-171	-171	-171	-171	-171
K_3 (GPa)	208	208	208	208	208	208	208
f_s	0.004	0.004	0.004	0.004	0.004	0.004	0.004

3.2 Validation of FE analysis

3.2.1 Comparison of impact simulations and tests

The modified H-J-C constitutive model presented in the previous section is used in the FE simulations. The impact stress-strain responses and failure modes of the RULCC are compared. Figs.10 (a)-(g) compare the stress-strain relations measured from the tests with those from the simulations of the RULCC with varying strain rates. It is found that for the RULCC, the simulation results agree very well with the test ones, especially when the content of PE fibers is low, which indicates that the modified H-J-C constitutive model with the newly calibrated parameters is capable of capturing satisfactorily the stress-strain responses of the novel rubberized concrete. Detailed comparisons of the numerical simulations and the SHPB test results are shown in Table 4, which shows that the predicted peak stresses and strain rates are in good agreement with the test results with an average difference of less than 2.91%, and 4.51%, respectively.

Table 4 Comparison of test and simulation

MIX ID	SCS /MPa	Test				Numerical simulation				Difference		
		DIS /MPa	DPS	SR (/s)	DIF	DIS /MPa	DPS	SR (/s)	DIF	DIS	DPS	SR
R0-0	52.20	79.70	4203	94.10	1.53	80.12	5206	96.70	1.53	0.53%	23.86%	2.76%
		88.70	2112	130.60	1.70	88.16	2030	121.30	1.69	0.61%	3.88%	7.12%
		96.40	2267	150.70	1.85	96.71	2309	154.60	1.85	0.32%	1.85%	2.59%
		100.80	3467	183.40	1.93	102.43	3480	199.60	1.96	1.62%	0.37%	8.83%
R0-0.7PE	43.50	68.00	4312	102.10	1.56	70.26	4627	96.70	1.62	3.32%	7.31%	5.29%
		76.30	3601	128.30	1.75	78.07	3843	117.30	1.79	2.32%	6.71%	8.57%
		97.30	5778	146.80	2.24	97.75	6219	147.70	2.25	0.46%	7.63%	0.61%
		117.50	5734	166.40	2.70	115.86	6370	159.60	2.66	1.40%	11.09%	4.09%
R5-0	36.80	76.30	3948	91.90	2.07	75.35	3849	97.30	2.05	1.25%	2.50%	5.88%
		91.20	5515	123.40	2.48	87.17	5499	114.70	2.37	4.42%	0.30%	7.05%
		93.70	7838	149.90	2.55	94.85	6337	156.70	2.58	1.23%	19.15%	4.54%
		95.80	7527	178.60	2.60	91.96	7167	175.60	2.50	4.01%	4.78%	1.68%
R10-0	27.30	49.60	4532	105.30	1.82	49.50	3264	100.60	1.81	0.20%	27.98%	4.46%
		62.10	3964	128.40	2.27	63.53	4508	134.40	2.33	2.31%	13.72%	4.67%
		65.00	4631	155.70	2.38	65.24	4387	149.30	2.39	0.37%	5.27%	4.11%
		74.60	5506	181.50	2.73	73.00	7124	196.40	2.67	2.14%	29.38%	8.21%
R10-0.7PE	24.90	37.40	3236	93.10	1.50	35.08	1861	87.30	1.41	6.21%	42.50%	6.23%
		41.90	1242	138.20	1.68	40.63	2021	132.10	1.63	3.04%	62.73%	4.41%
		48.30	2002	158.70	1.94	48.45	2152	155.60	1.95	0.32%	7.47%	1.95%
		57.60	3140	185.10	2.31	59.80	2854	192.10	2.40	3.81%	9.11%	3.78%
R15-0	23.60	49.40	2644	104.80	2.09	50.66	1958	100.90	2.15	2.54%	25.93%	3.72%
		50.30	4567	129.20	2.13	46.61	1722	119.70	1.97	7.35%	62.29%	7.35%
		56.80	2561	159.80	2.41	58.58	2198	158.70	2.48	3.13%	14.18%	0.69%
		65.30	2391	180.90	2.77	67.93	2426	177.60	2.88	4.03%	1.44%	1.82%
R20-0	20.70	40.80	1938	99.70	1.97	35.37	2719	94.30	1.71	13.32%	40.29%	5.42%
		46.80	2107	123.50	2.26	48.16	2794	119.60	2.33	2.90%	32.59%	3.16%
		53.70	2696	150.50	2.59	55.63	2580	144.40	2.69	3.60%	4.29%	4.05%
		57.40	2650	186.50	2.77	60.06	2447	180.60	2.90	4.63%	7.68%	3.16%
Mean.										2.91%	17.01%	4.51%
Std.										0.027	0.177	0.023

Note: SCS=Static compressive strength; DIS=Dynamic impact strength; DPS=Dynamic peak strain; SR=Strain rate.

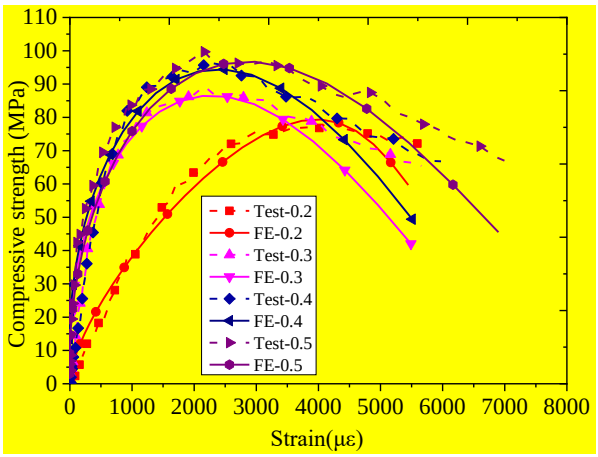

(a) R0-0

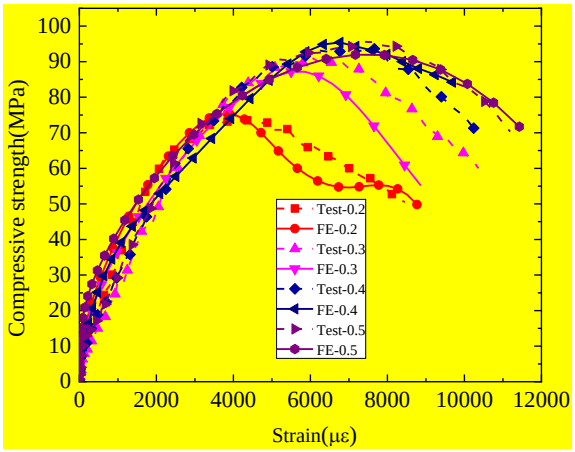

(b) R5-0

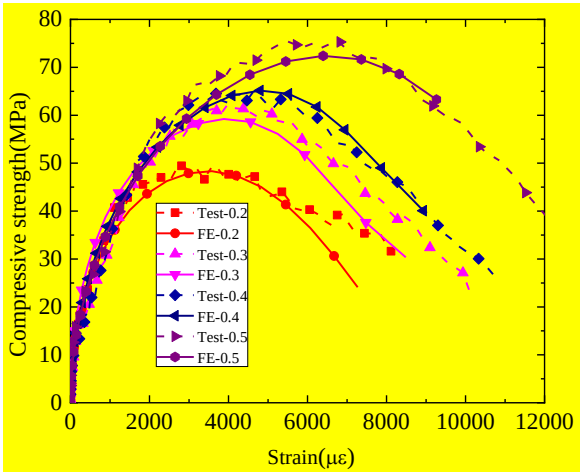

(c) R10-0

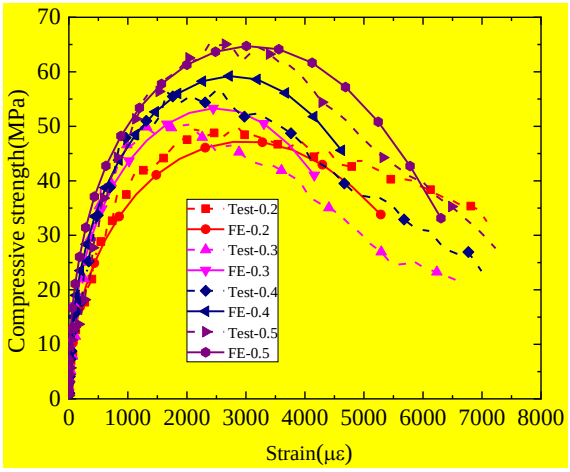

(b) R15-0

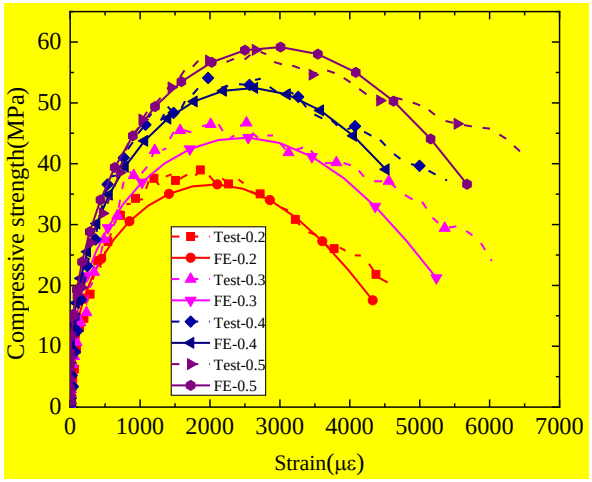

(e) R20-0

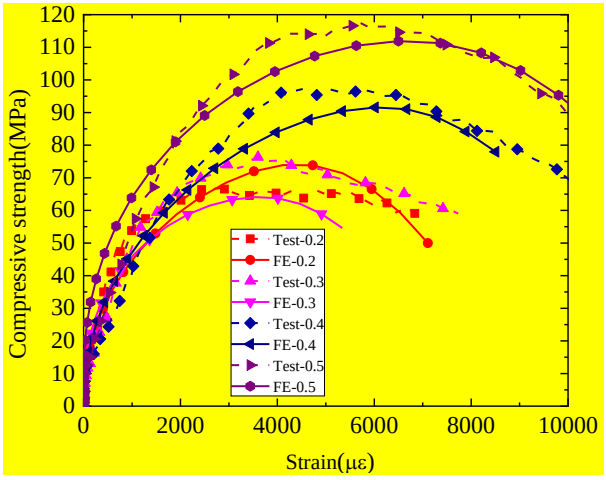

(f) R0-0.7PE

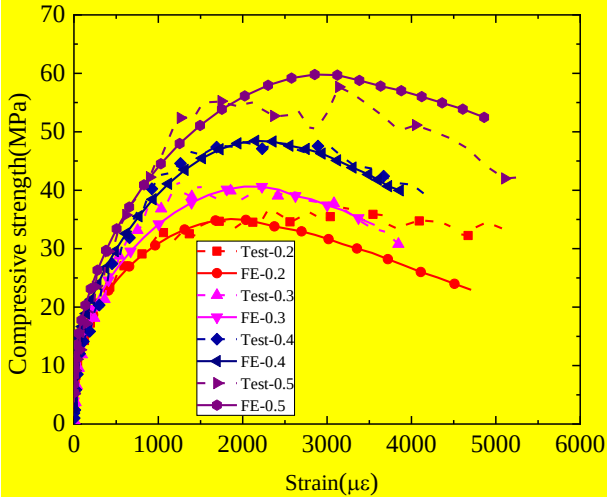

(g) R10-0.7PE

Fig.10 Comparison of stress-strain curves for different strain rates

3.2.2 Failure modes

Figure.11 illustrates the failure modes of the specimens R0-0, R10-0 and R0-0.7PE under the air pressures of 0.4MPa, 0.3MPa and 0.2MPa, respectively. The pictures were captured by a high speed camera at intervals within 0.00025 seconds from the start of the impact. It can be seen that the damage of the RULCC with added rubber (R10-0) and fibers (R0-0.7PE) is not as serious as that of R0-0. Figs.11 (a)-(c) also show the strain contours from the FE model, which are comparable to the damage shown in the images captured by the high-speed camera. The blue and red colors represent no damage and fully damaged, respectively. It can be seen from the contour plots of the predicted damage zone in Figs.11 (a)-(c) that the modified H-J-C FE model is able to reproduce the failure process and the damage of the RULCC specimens under high strain rate impact. Fig.12 shows the detected cracks in the FE model by removing elements whose strains have exceeded the maximum plastic strain of the material. In general, the numerical model provides reasonable estimations of the dynamic stress-strain curves for most of the tested specimens, including the maxi-

mum stress, damage initiation, failure process as well as the peak stresses and strain rates, as presented in Table 4. It can be concluded that the modified H-J-C constitutive model proposed in this study can be used to estimate the impact performance of the RULCC subjected to various loading strain rates. Thus, the validated model is used in the next section to generate data for metamodeling of the RULCC .

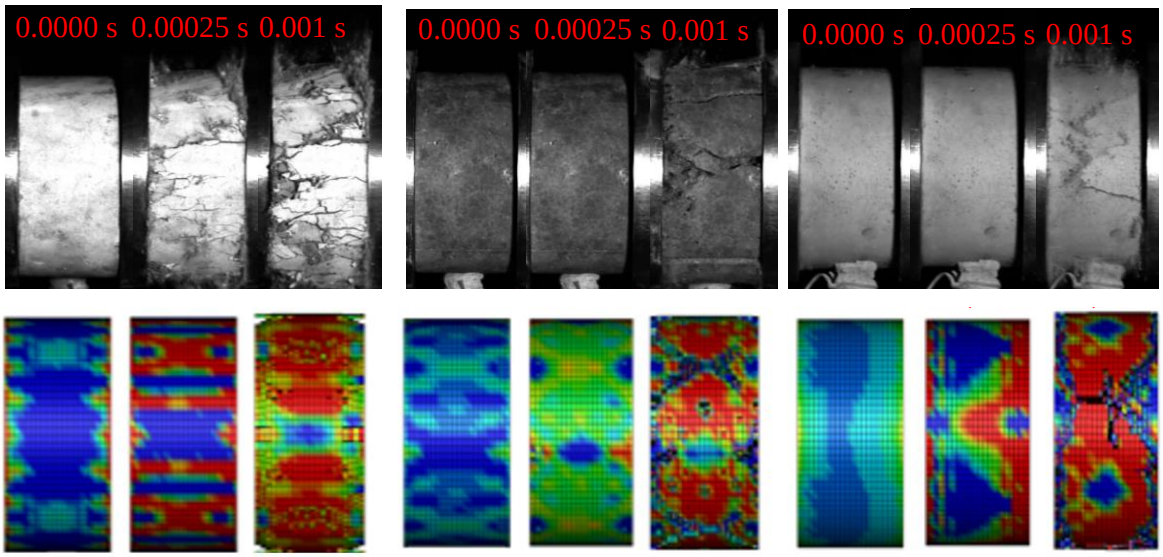

(a)R0-0(0.4MPa) (b)R10-0(0.3MPa) (c)R0-0.7PE(0.2MPa)

Fig.11 Comparison of failure modes between FE and tests

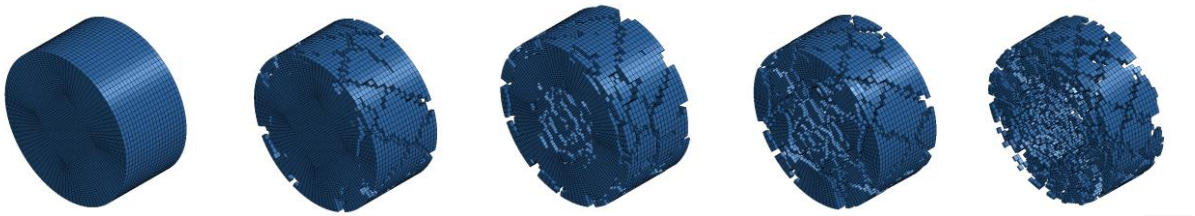

R0-0(No impact) R0-0(0.2MPa) R0-0(0.3MPa) R0-0(0.4MPa) R0-0(0.5MPa)

Time = 0.5ms

Fig.12 Failure of RULCC under different loading pressure

4. Data-driven model from metamodeling

It is evident that traditional engineering design processes may require expensive and labour intensive experimental tests, which may be ineffective and practically unaffordable. Benefiting from

387 the development of reliable and robust finite element analysis, such as the simulations presented
388 in the previous section, computer-aided-design has virtually replaced the traditional design pro-
389 cess, especially, of large scale and complex systems. However, due to the increase of design com-
390 plexities, a set of design variables have to be considered in order to assess a design, especially
391 when optimization is involve. This process may be prohibitively expensive. Thus, it is ideal if an
392 accurate and explicit meta-model (surrogate) can be used to replace the original FE simulations so
393 that a design can be evaluated based on simple algebraic calculations. In this section, a meta-
394 model is developed to evaluate the dynamic strength of the RULCC that have varying volume
395 ratios of rubber and fibers when they are subjected to varying impact strain rates.

396 **4.1 DoE sampling**

397 In order to construct an efficient meta-model, design of experiment (DoE) is used to effectively
398 select sampling points in the design space for data acquisition. In this paper, a uniform Latin hy-
399 percube DoE based on the use of the Audze-Eglais criterion is used to explore the design space
400 with reduced sampling points, which minimizes the function, U, defined in Eq.(21), using the
401 squared Euclidean distances between all pairs of experimental points

402 $$U = \sum_{p=1}^{P} \sum_{q=p+1}^{P} \frac{1}{L_{pq}^2} \tag{21}$$

403 where, P is the total number of points, L_{pq} is the Euclidean distance between points p and q ($p \neq q$).
404 In this study the effect of the volume ratios of rubber and fibesr on the impact strength of the
405 material under varying strain rates is investigated. Hence, bounds are set on these three variables
406 to cover a range of the materials for different engineering applications, as shown in Table 5.

407 Table 5 Bounds of design variables

Design Variables	Lower bound	Upper Bound
Fiber contents (%)	0	0.7

Rubber contents (%)	0	20
Strain rates (/s)	20	200

After some initial tests on the sampling process and comparisons with the experimental results, it is decided that 60 representative designs of the materials, which are determined by 60 almost equally spaced sampling points in the design space specified in Table 5, are used for the development of the meta-model. Details of the 60 designs, which are the 3D spatial point locations defined in the fiber ratio-rubber ratio-strain rate space, is given in the Appendix. Fig.13 illustrates the uniformness of the distribution of the sampling points (designs) within the design space by calculating the minimum Euclidean distance between each of the points to their surrounding points, i.e.,

$$D_{\min}^{i} = \min\{L_{ij}\} \qquad j = 1,2,\ldots i-1, i+1,\ldots n \tag{22}$$

where $D_{\min}^{i}$ is the minimum distance from point i (=1,….60) to all the surrounding points. The L_{ij} are the Euclidean distances calculated after Eq.(22) is minimized. Fig.13 shows that a reasonable uniform spacing has been achieved.

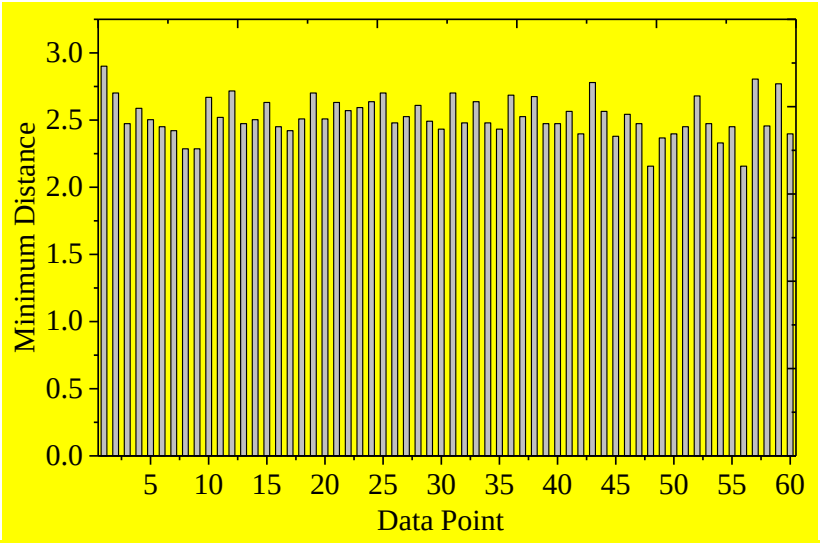

Fig.13 Minimum distances between points generated by OLH within the design space

4.2 Data generation

The required data for the DoE selected sampling points (designs) are generated in this section using the experimentally validated H-J-C model presented in Section 3.1. At the selected sampling points, the material properties, such as the compressive strength, elastic modulus and tensile strength, are obtained by solving multiple nonlinear functions through Levenberg Marquardt method based on the laboratory database [56]. The remaining parameters including A, B, P_c and u_c are calculated by the state equation, the hydraulic pressure volume relationship and the damage evolution equation shown in Section 3.1. A summary of all the parameters used in the FE simulations of the 60 designs are presented in Table 6. The computation of the 60 models was completed using a cloud computing platform, where a multi node cloud simulation framework was built, as shown by the flowchart in Fig.14. The multi model calculation based on the elastic scaling work and the multi-server method has demonstrated that the process is effective and efficient in terms of both the computing time and the laboratory resources.

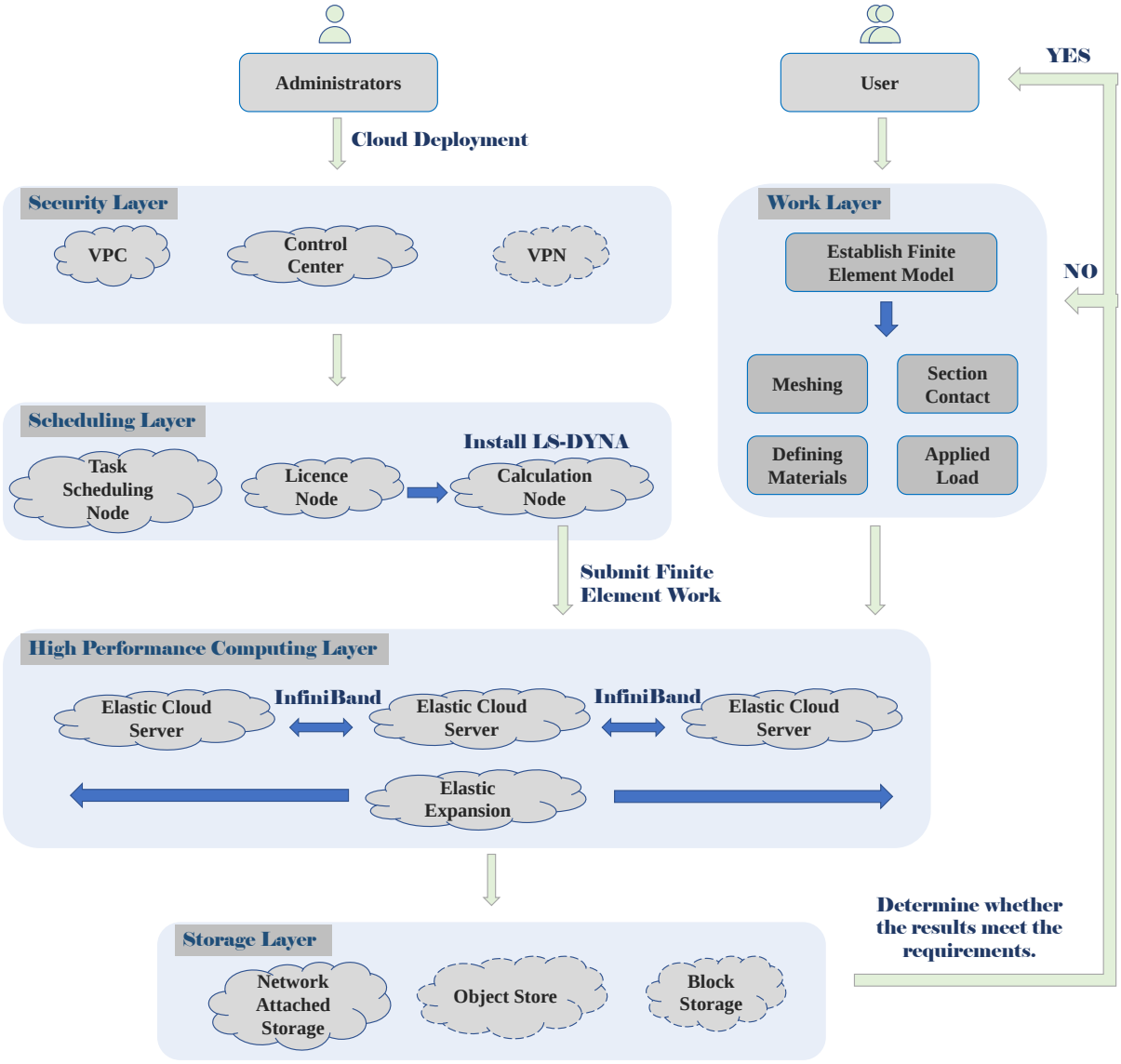

435

436 Fig.14 Multi node cloud simulation framework based on cloud platform

437

Table 6 Parameters of HJC model for extended FE simulation

Material	Density ρ (kg/m^3)	G (GPa)	A	B	C	N	f_c (MPa)	T (MPa)	$\dot{\varepsilon}_0$	εf_{min}	S_{max}	P_c (MPa)	μ_c	P_1 (GPa)	μ_1	D_1	D_2	K_1 (GPa)	K_2 (GPa)	K_3 (GPa)	f_s
No.1	1400	4.848	0.55	2.33	0.007	1.36	41.2	2.0	1	0.01	7	13.73	0.0021246	0.9	0.12	0.04	1	85	-171	208	0.004
No.2	1400	4.332	0.50	2.20	0.007	1.36	25.5	1.72	1	0.01	7	8.51	0.0014737	0.9	0.12	0.04	1	85	-171	208	0.004
No.3	1400	4.421	0.50	2.21	0.007	1.36	27.4	1.76	1	0.01	7	9.12	0.0015475	0.9	0.12	0.04	1	85	-171	208	0.004
No.4	1400	4.477	0.50	2.21	0.007	1.36	28.8	1.79	1	0.01	7	9.61	0.0016092	0.9	0.12	0.04	1	85	-171	208	0.004
No.5	1400	5.050	0.54	2.24	0.007	1.36	40.0	2.06	1	0.01	7	13.33	0.0019796	0.9	0.12	0.04	1	85	-171	208	0.004
No.6	1400	4.945	0.53	2.24	0.007	1.36	38.2	2.01	1	0.01	7	12.73	0.0019302	0.9	0.12	0.04	1	85	-171	208	0.004
No.7	1400	5.098	0.54	2.25	0.007	1.36	41.3	2.08	1	0.01	7	13.77	0.0020256	0.9	0.12	0.04	1	85	-171	208	0.004
No.8	1400	3.832	0.47	2.14	0.007	1.36	21.1	1.48	1	0.01	7	7.02	0.0013742	0.9	0.12	0.04	1	85	-171	208	0.004
No.9	1400	3.889	0.47	2.15	0.007	1.36	21.7	1.51	1	0.01	7	7.23	0.0013950	0.9	0.12	0.04	1	85	-171	208	0.004
No.10	1400	3.558	0.45	2.11	0.007	1.36	17.8	1.35	1	0.01	7	5.94	0.0012522	0.9	0.12	0.04	1	85	-171	208	0.004
No.11	1400	4.711	0.52	2.22	0.007	1.36	34.8	1.90	1	0.01	7	11.60	0.0018460	0.9	0.12	0.04	1	85	-171	208	0.004
No.12	1400	3.994	0.48	2.15	0.007	1.36	23.2	1.56	1	0.01	7	7.72	0.0014494	0.9	0.12	0.04	1	85	-171	208	0.004
No.13	1400	5.275	0.55	2.27	0.007	1.36	44.7	2.16	1	0.01	7	14.89	0.0021170	0.9	0.12	0.04	1	85	-171	208	0.004
No.14	1400	4.622	0.52	2.21	0.007	1.36	33.6	1.85	1	0.01	7	11.19	0.0018156	0.9	0.12	0.04	1	85	-171	208	0.004
No.15	1400	4.743	0.52	2.22	0.007	1.36	35.8	1.91	1	0.01	7	11.92	0.0018853	0.9	0.12	0.04	1	85	-171	208	0.004
No.16	1400	4.252	0.50	2.17	0.007	1.36	27.4	1.68	1	0.01	7	9.14	0.0016131	0.9	0.12	0.04	1	85	-171	208	0.004
No.17	1400	5.340	0.56	2.28	0.007	1.36	45.7	2.19	1	0.01	7	15.25	0.0021415	0.9	0.12	0.04	1	85	-171	208	0.004
No.18	1400	3.687	0.46	2.09	0.007	1.36	18.8	1.41	1	0.01	7	6.25	0.0012721	0.9	0.12	0.04	1	85	-171	208	0.004
No.19	1400	4.098	0.49	2.14	0.007	1.36	25.1	1.60	1	0.01	7	8.37	0.0015314	0.9	0.12	0.04	1	85	-171	208	0.004
No.20	1400	5.122	0.55	2.27	0.007	1.36	42.4	2.09	1	0.01	7	14.14	0.0020704	0.9	0.12	0.04	1	85	-171	208	0.004
No.21	1400	3.566	0.46	2.06	0.007	1.36	16.9	1.35	1	0.01	7	5.65	0.0011874	0.9	0.12	0.04	1	85	-171	208	0.004

No.22	1400	4.106	0.49	2.14	0.007	1.36	25.4	1.61	1	0.01	7	8.46	0.0015456	0.9	0.12	0.04	1	85	-171	208	0.004
No.23	1400	4.937	0.54	2.25	0.007	1.36	39.5	2.00	1	0.01	7	13.17	0.0020011	0.9	0.12	0.04	1	85	-171	208	0.004
No.24	1400	4.026	0.48	2.12	0.007	1.36	24.1	1.57	1	0.01	7	8.05	0.0014991	0.9	0.12	0.04	1	85	-171	208	0.004
No.25	1400	5.050	0.54	2.27	0.007	1.36	41.4	2.05	1	0.01	7	13.81	0.0020507	0.9	0.12	0.04	1	85	-171	208	0.004
No.26	1400	3.558	0.46	2.04	0.007	1.36	16.7	1.35	1	0.01	7	5.57	0.0011733	0.9	0.12	0.04	1	85	-171	208	0.004
No.27	1400	4.389	0.51	2.17	0.007	1.36	30.4	1.74	1	0.01	7	10.15	0.0017342	0.9	0.12	0.04	1	85	-171	208	0.004
No.28	1400	4.477	0.51	2.18	0.007	1.36	32.0	1.78	1	0.01	7	10.67	0.0017875	0.9	0.12	0.04	1	85	-171	208	0.004
No.29	1400	4.534	0.52	2.19	0.007	1.36	33.0	1.81	1	0.01	7	11.01	0.0018211	0.9	0.12	0.04	1	85	-171	208	0.004
No.30	1400	5.203	0.55	2.30	0.007	1.36	43.9	2.12	1	0.01	7	14.65	0.0021112	0.9	0.12	0.04	1	85	-171	208	0.004
No.31	1400	3.421	0.45	1.99	0.007	1.36	14.5	1.28	1	0.01	7	4.84	0.0010600	0.9	0.12	0.04	1	85	-171	208	0.004
No.32	1400	3.929	0.48	2.09	0.007	1.36	22.8	1.52	1	0.01	7	7.61	0.0014522	0.9	0.12	0.04	1	85	-171	208	0.004
No.33	1400	4.759	0.53	2.23	0.007	1.36	37.0	1.91	1	0.01	7	12.33	0.0019431	0.9	0.12	0.04	1	85	-171	208	0.004
No.34	1400	5.235	0.56	2.32	0.007	1.36	44.5	2.14	1	0.01	7	14.84	0.0021255	0.9	0.12	0.04	1	85	-171	208	0.004
No.35	1400	3.776	0.47	2.05	0.007	1.36	20.3	1.45	1	0.01	7	6.78	0.0013458	0.9	0.12	0.04	1	85	-171	208	0.004
No.36	1400	3.703	0.47	2.03	0.007	1.36	19.1	1.41	1	0.01	7	6.38	0.0012913	0.9	0.12	0.04	1	85	-171	208	0.004
No.37	1400	3.824	0.48	2.06	0.007	1.36	21.2	1.47	1	0.01	7	7.07	0.0013865	0.9	0.12	0.04	1	85	-171	208	0.004
No.38	1400	4.751	0.53	2.24	0.007	1.36	37.0	1.91	1	0.01	7	12.35	0.0019492	0.9	0.12	0.04	1	85	-171	208	0.004
No.39	1400	4.227	0.50	2.14	0.007	1.36	28.2	1.66	1	0.01	7	9.41	0.0016697	0.9	0.12	0.04	1	85	-171	208	0.004
No.40	1400	4.993	0.55	2.29	0.007	1.36	41.0	2.02	1	0.01	7	13.66	0.0020516	0.9	0.12	0.04	1	85	-171	208	0.004
No.41	1400	3.276	0.45	1.92	0.007	1.36	12.1	1.21	1	0.01	7	4.02	0.0009210	0.9	0.12	0.04	1	85	-171	208	0.004
No.42	1400	5.074	0.55	2.31	0.007	1.36	42.3	2.06	1	0.01	7	14.09	0.0020829	0.9	0.12	0.04	1	85	-171	208	0.004
No.43	1400	4.550	0.52	2.20	0.007	1.36	33.9	1.81	1	0.01	7	11.30	0.0018622	0.9	0.12	0.04	1	85	-171	208	0.004
No.44	1400	4.606	0.52	2.22	0.007	1.36	34.9	1.84	1	0.01	7	11.62	0.0018925	0.9	0.12	0.04	1	85	-171	208	0.004
No.45	1400	4.308	0.51	2.15	0.007	1.36	29.9	1.69	1	0.01	7	9.96	0.0017334	0.9	0.12	0.04	1	85	-171	208	0.004
No.46	1400	4.106	0.50	2.11	0.007	1.36	26.4	1.60	1	0.01	7	8.81	0.0016091	0.9	0.12	0.04	1	85	-171	208	0.004

No.47	1400	3.647	0.47	1.99	0.007	1.36	18.5	1.38	1	0.01	7	6.15	0.0012648	0.9	0.12	0.04	1	85	-171	208	0.004
No.48	1400	3.478	0.46	1.95	0.007	1.36	15.5	1.30	1	0.01	7	5.18	0.0011168	0.9	0.12	0.04	1	85	-171	208	0.004
No.49	1400	3.308	0.45	1.90	0.007	1.36	12.6	1.22	1	0.01	7	4.21	0.0009545	0.9	0.12	0.04	1	85	-171	208	0.004
No.50	1400	3.752	0.48	2.01	0.007	1.36	20.4	1.43	1	0.01	7	6.79	0.0013580	0.9	0.12	0.04	1	85	-171	208	0.004
No.51	1400	4.163	0.50	2.12	0.007	1.36	27.6	1.62	1	0.01	7	9.20	0.0016580	0.9	0.12	0.04	1	85	-171	208	0.004
No.52	1400	4.413	0.51	2.18	0.007	1.36	31.9	1.74	1	0.01	7	10.64	0.0018087	0.9	0.12	0.04	1	85	-171	208	0.004
No.53	1400	4.921	0.54	2.31	0.007	1.36	40.2	1.98	1	0.01	7	13.40	0.0020429	0.9	0.12	0.04	1	85	-171	208	0.004
No.54	1400	4.751	0.54	2.27	0.007	1.36	37.6	1.90	1	0.01	7	12.52	0.0019769	0.9	0.12	0.04	1	85	-171	208	0.004
No.55	1400	3.357	0.45	1.90	0.007	1.36	13.6	1.24	1	0.01	7	4.52	0.0010106	0.9	0.12	0.04	1	85	-171	208	0.004
No.56	1400	4.767	0.54	2.28	0.007	1.36	37.9	1.91	1	0.01	7	12.63	0.0019869	0.9	0.12	0.04	1	85	-171	208	0.004
No.57	1400	3.470	0.46	1.92	0.007	1.36	15.6	1.29	1	0.01	7	5.20	0.0011250	0.9	0.12	0.04	1	85	-171	208	0.004
No.58	1400	3.945	0.49	2.06	0.007	1.36	24.1	1.52	1	0.01	7	8.03	0.0015259	0.9	0.12	0.04	1	85	-171	208	0.004
No.59	1400	4.163	0.50	2.12	0.007	1.36	27.9	1.62	1	0.01	7	9.31	0.0016766	0.9	0.12	0.04	1	85	-171	208	0.004
No.60	1400	4.445	0.52	2.20	0.007	1.36	32.8	1.75	1	0.01	7	10.92	0.0018423	0.9	0.12	0.04	1	85	-171	208	0.004

438

4.3 Meta-model building by Genetic Programming (GP)

Genetic programming (GP) is used in this paper to select a structure of high-quality global approximations to the predictions of the dynamic strength of the composites that fall within the design space set in Table 5. Unlike building empirical model which is usually problematic in selecting the structure of the approximation function, GP searches for the structure by following an effective tree structure, as shown in the flowchart in Fig.15 for a typical expression of $\left(x_1 \times x_2 - x_3\right)^2$. The process starts with an introduction of the parameters. The fitness is evaluated then to determine the quality of the approximations of the current generations. A poor fitness value will activate tuning algorithms. The common tuning algorithms used in GP are reproduction, mutation and crossover, which perform on the connections between mathematical operators and the terminal nodes. The whole process terminates only when the fitness reaches an acceptable level.

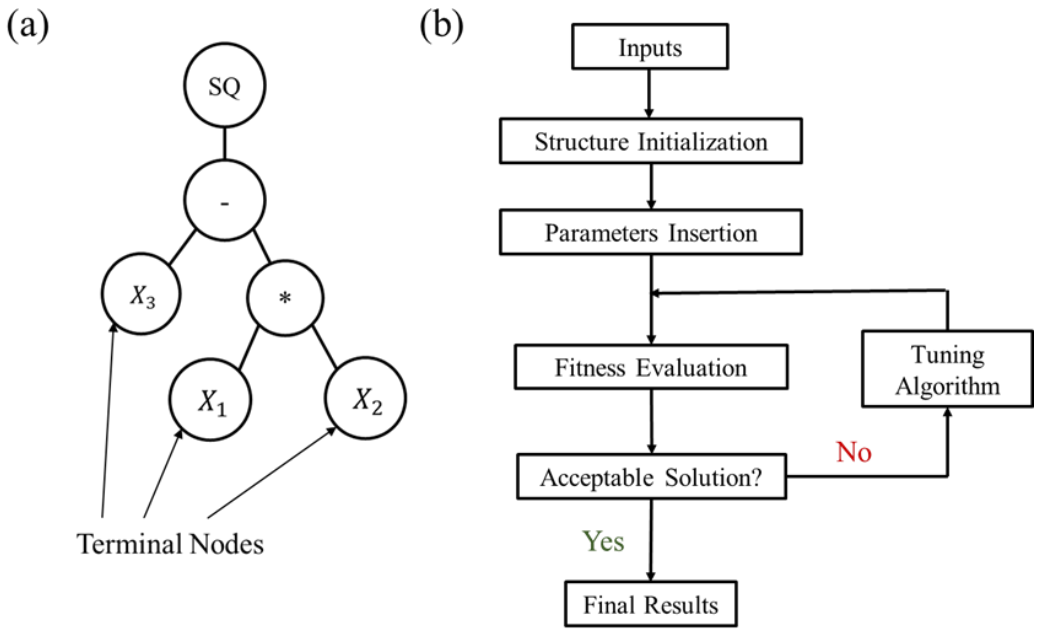

Fig.15 (a) Tree structure for the expression $\left(x_1 \times x_2 - x_3\right)^2$, (b) a brief flowchart of genetic programming process

After implementing the above meta-modeling procedures and conducting the FE simulations for the 60 sampling results, the following analytical expression are found, as presented in Eq.(23).

$$DIS = 1.43 f_1 - 0.68 f_4 - 1.82 V_r - 0.32 \dot{\varepsilon} + \sqrt{|1.43 f_7 - \dot{\varepsilon}|} \quad (23)$$

where $f_1 = \sqrt{(69 - V_r)\dot{\varepsilon}}$, $f_2 = \sqrt{\frac{\dot{\varepsilon}}{1+V_r} + V_f}$, $f_3 = \dot{\varepsilon} \cdot V_f - \sqrt{V_r}$, $f_4 = \frac{f_3}{f_2}$, $f_5 = \sqrt{V_r}(12 - \sqrt{\dot{\varepsilon}})$,

$f_6 = (\dot{\varepsilon} - \sqrt{\dot{\varepsilon}}) \cdot \frac{f_5 \cdot \dot{\varepsilon}}{f_5 + V_r}$, $f_7 = \sqrt{|70(\dot{\varepsilon} + V_r) - f_6|}$.

In Eq.(23), *DIS* denotes Dynamic Impact Strength of the RULCC, V_f, V_r and $\dot{\varepsilon}$ are, respectively, the fiber ratio, the rubber ratio and the dynamic strain rate.

Fig.16 presents the comparisons between the dynamic strength of the RULCC predicted by the simple meta-model (Eq.23) and those from the experimental tests and the FE simulations.

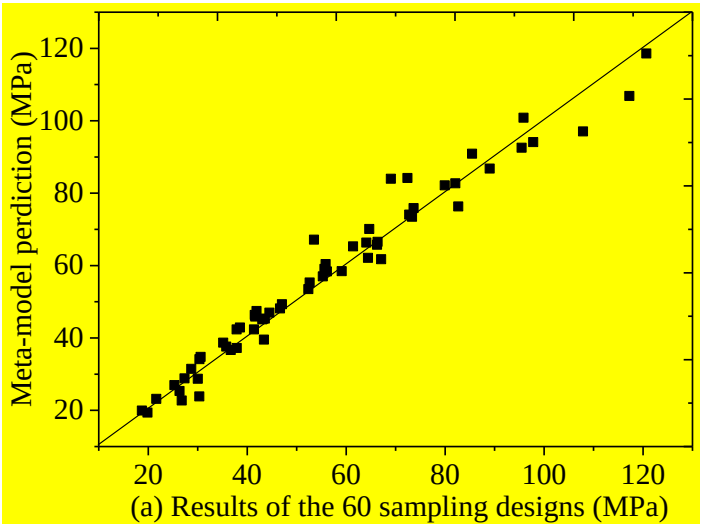

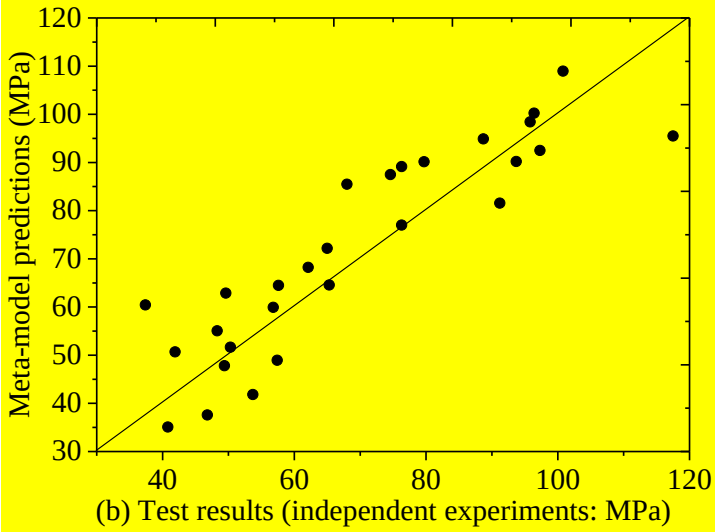

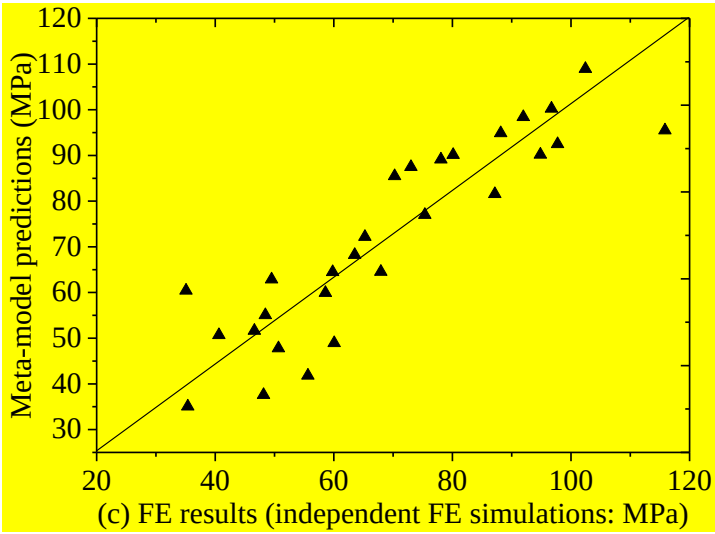

Fig.16 Comparisons between the metamodeling predictions and (a) Experimental and FE results used in the data training process, (b) Independent experimental results, and (c) Independent finite element results.

Figure.16(a) compares the predicted dynamic strength using Eq.(23) with the strength of the 60 designs selected by the DoE. The FE simulation results of the 60 samples were used in the data training process. The comparisons demonstrate that the meta-model approximates the FE models very well. To further validate the meta-model, dynamic strength of the RULCC from Eq.(23) are compared with those from independent experiment results and FE simulations (not used in the data training process) in Fig.16(b) and Fig.16(c), respectively. Evidently, the meta-model is sufficiently

accurate in predicting dynamic strength of the RULCC with a range of fiber or/and rubber reinforcement ratios, and subjected to different dynamic strain rates. It is worth of stressing that by using Eq.(23), only simple hand calculations or a programmable calculator are required to replace costing experimental tests or/and sophisticated FE simulations.

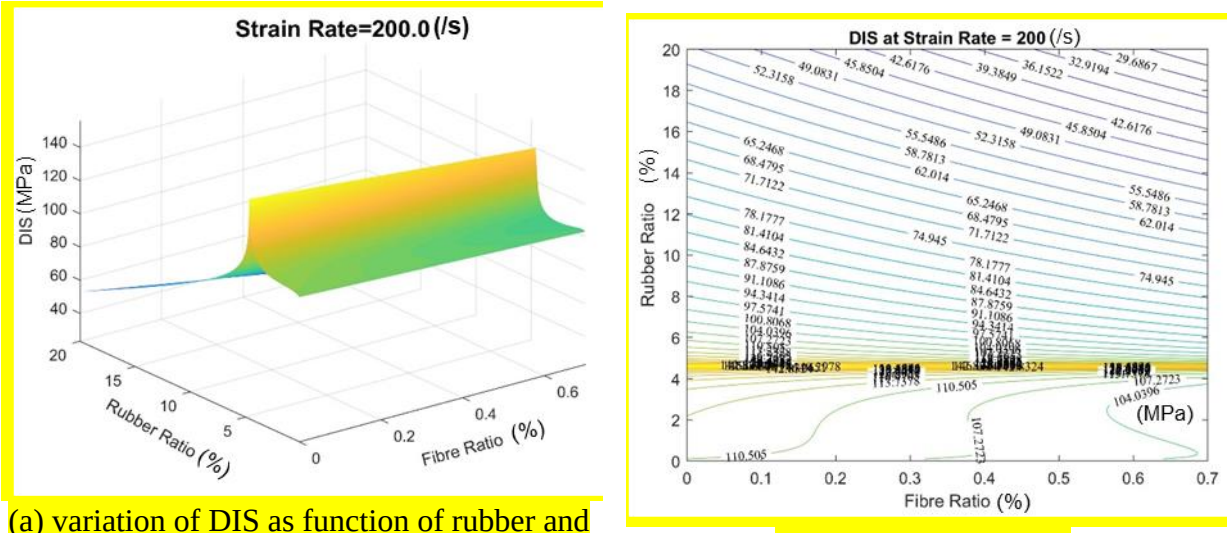

(a) variation of DIS as function of rubber and fiber ratios

(b) contour plot of DIS

Fig.17. DIS of the RULCC at impact strain rate of 200/s

Figure 17 presents a snapshot and the contour plot of the DIS at a strain rate of 200/s for varying fiber and rubber ratios. The contour plot shows that the RULCC has a maximum DIS when the rubber ratio is somewhere between 4~5%. Above this ratio, any increase of rubber ratio will reduce the DIS. Hence, a proportional increase of fiber ratio is required to maintain the strength. When the rubber ratio is smaller than this threshold, to maintain the dynamic strength at a certain level, an increase of rubber ratio may require an increase of fiber ratio as well.

5. Conclusions

This study developed a modified constitutive law for lightweight cement composite with added rubber or/and fibers, based on the H-J-C constitutive model that was developed for normal concrete.

New SHPB experimental tests on a novel rubberized ultra-lightweight high-ductility cement composite (RULCC) were carried out and comparisons were made between the test results and the FE simulations using the modified constitutive law.

To facilitate the assessment and design of the RULCC, a simple and practical design formula was proposed to predict the dynamic impact strength of the material using a data-driven meta-modeling process. To reduce the amount of data required in the data training process, the unified Latin hypercube DoE based on Audze-Eglais criterion was used to collect sampling points. An explicit formula was then developed from genetic programming, which can predict the dynamic impact strength (DIS) of the RULCC with full consideration of the interactions between fiber ratio, rubber ratio and impact strain rate. The formula is the first of its kind and can be easily implemented in a design process using hand calculation or a programmable calculator.

In a general term, the methods adopted and developed in this study can be used in many other areas of engineering to develop better and more inclusive design formulas.

This work reported in this paper was concentrated on achieving an appropriate balance of strength, density and ductility without considering the environmental impact of using high quantity cement. Future work includes reduction of the cement content in the RULCC to reduce the impact on the sustainable construction. The ongoing work is to replace cement with supplementary cementitious materials (SCMs), e.g., calcined clay [69], ground granulated blast-furnace slag (GGBS) [70], etc., which appears to be among the most economical and effective approach to develop sustainable construction materials. The method developed in this paper will play an important role in evaluate the performance of these new materials.

Acknowledgement

The authors would like to acknowledge the research grant received from the National Natural Science Foundation of China (NSFC, No.51708360, No.51978407), Shenzhen Basic Research

Project (NO. JCYJ20180305124106675) and Shenzhen University Teaching Reform Research Project for Young Teachers (JG2018094).

References

[1] Noaman AT, Bakar BA, Akil HM. Experimental investigation on compression toughness of rubberized steel fibre concrete. Construction and Building Materials. 2016;115:163-70.

[2] Ho AC, Turatsinze A, Hameed R, Vu DC. Effects of rubber aggregates from grinded used tyres on the concrete resistance to cracking. Journal of Cleaner Production. 2012;23:209-15.

[3] da Silva L, Benta A, Picado-Santos L. Asphalt rubber concrete fabricated by the dry process: Laboratory assessment of resistance against reflection cracking. Construction and Building Materials. 2018;160:539-50.

[4] Thomas BS, Kumar S, Mehra P, Gupta RC, Joseph M, Csetenyi LJ. Abrasion resistance of sustainable green concrete containing waste tire rubber particles. Construction and Building Materials. 2016;124:906-9.

[5] Gesoğlu M, Güneyisi E, Khoshnaw G, İpek S. Abrasion and freezing–thawing resistance of pervious concretes containing waste rubbers. Construction and Building Materials. 2014;73:19-24.

[6] Zheng L, Huo XS, Yuan Y. Experimental investigation on dynamic properties of rubberized concrete. Construction and Building Materials. 2008;22:939-47.

[7] Xue J, Shinozuka M. Rubberized concrete: A green structural material with enhanced energy-dissipation capability. Construction and Building Materials. 2013;42:196-204.

[8] Wang R, Gao P, Tian M, Dai Y. Experimental study on mechanical and waterproof performance of lightweight foamed concrete mixed with crumb rubber. Construction and Building Materials. 2019;209:655-64.

[9] Jung K-C, Roh I-T, Chang S-H. Thermal behavior and performance evaluation of epoxy-based polymer concretes containing silicone rubber for use as runway repair materials. Composite Structures. 2015;119:195-205.

[10] Jung K-C, Roh I-T, Chang S-H. Stress analysis of runway repaired using compliant polymer concretes with consideration of cure shrinkage. Composite Structures. 2015;119:13-23.

[11] Liu F, Chen G, Li L, Guo Y. Study of impact performance of rubber reinforced concrete. Construction and Building Materials. 2012;36:604-16.

[12] Abdelmonem A, El-Feky M, Nasr E-SA, Kohail M. Performance of high strength concrete containing recycled rubber. Construction and Building Materials. 2019;227:116660.

[13] Maho B, Sukontasukkul P, Jamnam S, Yamaguchi E, Fujikake K, Banthia N. Effect of rubber insertion on impact behavior of multilayer steel fiber reinforced concrete bulletproof panel. Construction and Building Materials. 2019;216:476-84.

[14] Huang Z, Liew JYR. Structural behaviour of steel-concrete-steel sandwich composite wall subjected compression and end moment. Thin-walled Structures 2016; 98: 592-606.

[15] Huang Z, Liew JY. Compressive resistance of steel-concrete-steel composite wall with J-hook connectors. Journal of Constructional Steel Research 2016;124: 142-162.

[16] Huang Z, Zhou Y, Hu G, Deng W, Gao H, Sui L. Flexural resistance and deformation be-havior of CFRP-ULCC-steel sandwich composite structures. Composite structures.2020. 28 Sep 2020. (Accepted)

[17] Fedroff D, Ahmad S, Savas BZ. Mechanical properties of concrete with ground waste tire rubber. Transportation Research Record. 1996;1532:66-72.

[18] Taha MMR, Eldieb AS, Elwahab MAA, Abdelhameed ME. Mechanical, Fracture, and Microstructural Investigations of Rubber Concrete. Journal of materials in Civil Engineering. 2008;20:640-9.

[19] Duarte APC, Silva BA, Silvestre N, De Brito J, Julio E, Castro JM. Tests and design of short steel tubes filled with rubberised concrete. Engineering Structures. 2016;112:274-86.

[20] Thomas BS, Gupta RC. Properties of high strength concrete containing scrap tire rubber. Journal of Cleaner Production. 2016;113:86-92.

[21] Liu RX, Hou WS, Yong-Hong XU, Kai-Sheng XU. Effect of Crumb Rubber on the Mechanical Properties of Concrete(in Chinese). Journal of Building Materials. 2009;12:341-4.

[22] Senin MS, Shahidan S, Abdullah SR, Guntor NA, Leman AS. A review on the suitability of rubberized concrete for concrete bridge decks. Iop Conference. 2017;271.

[23] Ganjian E, Khorami M, Maghsoudi AA. Scrap-tyre-rubber replacement for aggregate and filler in concrete. Construction and Building Materials. 2009;23:1828-36.
[24] Zheng L, Huo XS, Yuan Y. Strength, Modulus of Elasticity, and Brittleness Index of Rubberized Concrete(in Chinese). Journal of materials in Civil Engineering. 2008;20:692-9.
[25] Siddika A, Mamun MA, Alyousef R, Amran YHM, Aslani F, Alabduljabbar H. Properties and utilizations of waste tire rubber in concrete: A review. Construction and Building Materials. 2019;224:711-31.
[26] Guo YC, Liu F, Chen GX, Zeng GS. Experimental investigation on impact resistance of rubberized concrete(in Chinese). Journal of Building Materials. 2012;15:139-44.
[27] Dehdezi PK, Erdem S, Blankson MA. Physico-mechanical, microstructural and dynamic properties of newly developed artificial fly ash based lightweight aggregate – Rubber concrete composite. Composites Part B-engineering. 2015;79:451-5.
[28] Ali MAEM, Soliman AM, Nehdi ML. Hybrid-fiber reinforced engineered cementitious composite under tensile and impact loading. Materials & Design. 2017;117:139-49.
[29] ACI-544.2R-89. Measurement of properties of fiber reinforced concrete. USA: American Concrete Institute ACI, 1999.
[30] Zhao ZY, Qian BI, Wang LY. Plastical Cracking and Resistance to Impact for Rubber Partical Modified Cement-based Composites (in Chinese). China Concrete & Cement Products. 2008.
[31] Liu X M, Chia K S, Zhang M H, Liew J Y. Water and chloride ion penetration resistance of highstrength ultra lightweight cement composite. In: Proceedings ICDC 2012 International Congress on Durability of Concrete (ICDC2012). Norwegian Concrete Association, 2012.
[32] Huang Z, Liew JYR, Xiong M and Wang J, Structural behaviour of double skin composite system using ultra-lightweight cement composite. Construction and Building Materials 2015;86: 51-63.
[33] Huang Z, Liew JYR. Nonlinear finite element modelling and parametric study of curved steel–concrete–steel double skin composite panels infilled with ultra-lightweight cement composite. Construction and Building Materials 2015; 95:922-938.
[34] Huang Z, Wang J, Liew JYR and Marshall P. Lightweight steel-concrete-steel sandwich shell subject to punching shear. Ocean Engineering 2015; 102: 146-161.
[35] Liew JYR, Yan J, Huang Z. Steel-Concrete-Steel Sandwich Composite Structures-Recent Innovations. Journal of Constructional Steel Research.2017;130: 202-221.
[36] CEB-FIP. Model code 2010. Comite Euro-International du beton. 2010.
[37] CEB-FIP. Model code 1990. Comite Euro-International Du Beton, Paris. 1991:87-109.
[38] Zhou H, Brooks AL, Hanna D, Salarieh B. Thermal and Mechanical Properties of Cementitious Composites for Additive Construction of Energy-Saving Habitats. Earth and Space 2018: Engineering for Extreme Environments: American Society of Civil Engineers Reston, VA; 2018. p. 600-11.
[39] Zhang S. Influence of Pva Fiber and Steel Fiber on Mechanical Properties of New Cement Composites (in Chinese) [master]: Qingdao University of Technology, 2017.
[40] Chen G. Study on Impact Resistance of Rubber Concrete (in Chinese) [master]: Guangdong University of Technology, 2011.
[41] JSCE. Recommendations for design and construction of high performance fiber reinforced cement composites with multiple fine cracks (HPFRCC): Japan Society of Civil Engineers, Concrete Committee, 2008.
[42] Xiong B, Demartino C, Xiao Y. High-strain rate compressive behavior of CFRP confined concrete: Large diameter SHPB tests. Construction and Building Materials. 2019;201:484-501.
[43] Wang S, Zhang M-H, Quek ST. Mechanical behavior of fiber-reinforced high-strength concrete subjected to high strain-rate compressive loading. Construction and Building Materials. 2012;31:1-11.
[44] Lai J, Sun W. Dynamic behaviour and visco-elastic damage model of ultra-high performance cementitious composite. Cement and concrete research. 2009;39:1044-51.
[45] Chen Z, Yang Y, Yao Y. Quasi-static and dynamic compressive mechanical properties of engineered cementitious composite incorporating ground granulated blast furnace slag. Materials & Design. 2013;44:500-8.

[46] Huang Z, Sui L, Wang F, Du S, Zhou Y, Ye J. Dynamic compressive behavior of a novel ultra-lightweight cement composite incorporated with rubber powder. Composite Structures. 2020:112300.
[47] ASTM. C 39/C 39M.Standard Test method for compressive strength of cylindrical concrete specimens. West Conshohocken (PA): ASTM International.
[48] Halquist J. LS-DYNA keyword user's manual version 971. Livermore. CA: Liver-more Software Technology Corporation. 2007.
[49] Xu S-l, Chen C, Li Q-h, Zhao X. Numerical simulation on dynamic compressive behavior of ultra-high toughness cementitious composites. Engineering Mechanics. 2019:8.
[50] Kong X, Fang Q, Wu H, Peng Y. Numerical predictions of cratering and scabbing in concrete slabs subjected to projectile impact using a modified version of HJC material model. International journal of impact engineering. 2016;95:61-71.
[51] Polanco-Loria M, Hopperstad O, Børvik T, Berstad T. Numerical predictions of ballistic limits for concrete slabs using a modified version of the HJC concrete model. International journal of impact engineering. 2008;35:290-303.
[52] Yang H. Study on Dynamic Mechanical Behavior and Constitutive model of Fiber Reinforced Cemenitious Composites. (in Chinese) [Master]: South China University of Science and Engineering, 2016.
[53] Cao J. Dynamic Constitutive Model of Steel Fiber Reinforced Concrete and Its Finite Element. (in Chinese) [Doctor]: Southwest Jiaotong University, 2010.
[54] Ye ZB, Huang RY, Li YC, Lv L, Zhao K, Zhang YL, et al. Steel fiber-reinforced concrete under impact loading dynamic constitutive equation. Construction and Building Materials. 2018;190:1049-55.
[55] ASTM E11–01: Standard specification for wire cloth and sieves for testing purposes. ASTM Standards. 2001.
[56] Wang F. Study on dynamic properties of ultra lightweight cement composites modified by rubber powder (in Chinese) [Master]: Shenzhen University, 2020.
[57] Wu Y, Wang J-Y, Monteiro PJ, Zhang M-H. Development of ultra-lightweight cement composites with low thermal conductivity and high specific strength for energy efficient buildings. Construction and Building Materials. 2015;87:100-12.
[58] Johnson GR, Cook WH. A constitutive model and data for metals subjected to large strains, high strain rates and high temperatures. Engineering Fracture Mechanics. 1983;21:541-8.
[59] Ngo T, Mendis P, Krauthammer T. Behavior of ultrahigh-strength prestressed concrete panels subjected to blast loading. Journal of Structural Engineering. 2007;133:1582-90.
[60] Gupta T, Sharma RK, Chaudhary S. Impact resistance of concrete containing waste rubber fiber and silica fume. International journal of impact engineering. 2015;83:76-87.
[61] Holmquist TJ, Johnson GR. A computational constitutive model for glass subjected to large strains, high strain rates and high pressures. Journal of Applied Mechanics. 2011;78.
[62] Xu H, Wen H. A computational constitutive model for concrete subjected to dynamic loadings. International journal of impact engineering. 2016;91:116-25.
[63] Liu X, Chia KS, Zhang M-H. Development of lightweight concrete with high resistance to water and chloride-ion penetration. Cement and Concrete Composites. 2010;32:757-66.
[64] Qiyuan Li YH. Study on the inhomogeneity of spatial distribution of porosity in hardened cement paste.(in Chinese). Journal of Building Materials. 1994.
[65] Li Y. Research on HJC dynamic constitutive model for concrete. (in Chinese): Hefei Polytechnic University, 2009.
[66] Eurocode 2: Design of Concrete Structures-Part 1–2: General Rules-Structural Fire Design. Brussels: European Concrete Platform. 2004.
[67] Huang Z, Wang F, Zhou Y, Sui L, Krishnan P, Liew J-YR. A novel, multifunctional, floatable, lightweight cement composite: development and properties. Materials (Basel). 2018;11:2043.
[68] ASTM C469/C469M: Standard test method for static modulus of elasticity and Poisson's ratio of concrete in compression. Annual Book of ASTM Standards. 2014.

668 [69] Huang Z, Huang Y, Han N, Zhou Y, Xing F, Sui T, Wang B, Ma H. Development of lime-stone
669 calcined clay cement (LC3) concrete in South China and its bond behavior with steel bar. Journal of
670 Zhejiang University-SCIENCE A (Applied Physics & Engineering). 2020.21(1)
671 [70] Xie J, Wang J, Rao R, et al. Effects of combined usage of GGBS and fly ash on workabil-ity and
672 mechanical properties of alkali activated geopolymer concrete with recycled aggre-gate[J]. Composites,
673 2019, 164:179-190.
674

Appendix

The DoE selected fiber content ratios, rubber content ratios and dynamic strain rates of the 60 RULCC sampling designs are shown in Table A1.

Table A1 DoE selected fiber content ratios, rubber content ratios and dynamic strain rates of 60 RULCC materials

NO.	*fiber content (%)*	*rubber content (%)*	*strain rate (/s)*	NO.	*fiber content (%)*	*rubber content (%)*	*strain rate (/s)*
1	0	12.20339	44.40678	31	0.35593	13.89831	196.9492
2	0.01186	11.18644	166.4407	32	0.3678	5.08475	59.66102
3	0.02373	10.50847	105.4237	33	0.37966	0	93.22034
4	0.03559	4.40678	111.5254	34	0.39153	15.25424	29.15254
5	0.04746	5.42373	178.6441	35	0.40339	15.9322	99.32203
6	0.05932	3.72881	65.76271	36	0.41525	14.57627	148.1356
7	0.07119	16.94915	71.86441	37	0.42712	4.74576	120.678
8	0.08305	16.27119	160.339	38	0.43898	10.16949	90.16949
9	0.09492	19.66102	132.8814	39	0.45085	2.0339	172.5424
10	0.10678	7.45763	32.20339	40	0.46271	20	68.81356
11	0.11864	14.91525	117.6271	41	0.47458	1.01695	53.55932
12	0.13051	1.35593	154.2373	42	0.48644	6.44068	200
13	0.14237	8.13559	81.01695	43	0.49831	5.76271	23.05085
14	0.15424	6.77966	145.0848	44	0.51017	8.81356	138.9831
15	0.1661	11.86441	193.8983	45	0.52203	10.84746	47.45763
16	0.17797	0.33898	56.61017	46	0.5339	15.59322	190.8475
17	0.18983	17.62712	41.35593	47	0.54576	17.28814	38.30508
18	0.20169	13.22034	20	48	0.55763	18.98305	157.2881
19	0.21356	2.37288	102.3729	49	0.56949	14.23729	74.91525
20	0.22542	18.64407	87.11864	50	0.58136	9.83051	181.6949
21	0.23729	12.88136	151.1864	51	0.59322	7.11864	84.0678
22	0.24915	4.0678	26.10169	52	0.60508	1.69492	108.4746
23	0.26102	13.55932	77.9661	53	0.61695	3.38983	169.4915
24	0.27288	2.71186	187.7966	54	0.62881	17.9661	96.27119
25	0.28475	18.30508	175.5932	55	0.64068	3.05085	62.71186
26	0.29661	9.49153	50.50847	56	0.65254	16.61017	135.9322
27	0.30847	8.47458	123.7288	57	0.66441	11.52542	114.5763
28	0.32034	7.79661	184.7458	58	0.67627	9.15254	35.25424
29	0.3322	0.67797	142.0339	59	0.68814	6.10169	129.8305
30	0.34407	19.32203	126.7797	60	0.7	12.54237	163.3898